Preliminary Design Packet

Apical Robotics

Vedad Bassari, William Heap, Steven Man, Steven Nguyen, Rajveer Oberoi

March 13, 2022

Contents

1 Executive Summary **4**

2 Introduction **5**
2.1 Industrial Pipe Inspection . . . 5
2.1.1 Borescopes . . . 5
2.1.2 Inspection Robots . . . 5
2.2 Vine Robots . . . 6
2.2.1 Vine Robot Design . . . 6
2.3 Inspection Task and Target Specifications . . . 8

3 Theoretical Modeling **9**
3.1 Modeling Pressure and Tension in Growth . . . 10
3.2 Modeling Pressure and Tension in Retraction . . . 11
3.3 Buckling . . . 11
3.3.1 Constrained Buckling . . . 12
3.3.2 Unconstrained Buckling . . . 13
3.3.3 Crushing . . . 13
3.4 MATLAB Implementation of Theoretical Model . . . 13
3.5 Failure Modes in Growth and Retraction . . . 18
3.6 Material Selection . . . 18

4 Prototypes and Testing **20**
4.1 Base Station . . . 20
4.2 Experimental Characterization . . . 21
4.2.1 Yield Strength Testing . . . 22
4.2.2 Growth Testing . . . 22
4.2.3 Retraction Testing . . . 23
4.2.4 Buckling Testing . . . 25
4.3 Tip Mount . . . 26
4.4 Vine Robot Body . . . 26

5 Final Design **28**
5.1 Base Station v.2 . . . 28
5.1.1 Spool-motor Assembly . . . 28
5.1.2 Motor Selection . . . 29
5.1.3 Bag Sealing Method . . . 31
5.1.4 Intake Plate Assembly . . . 32
5.1.5 Back-plate Assembly . . . 32
5.1.6 Ethernet Cable Routing Assembly . . . 33
5.1.7 Baseplate . . . 33
5.1.8 Simulation-Based Optimization . . . 33
5.2 Tip Mount v.3 . . . 37
5.3 Fan Selection . . . 37
5.3.1 Fan Intake Mechanism . . . 37
5.4 Electronics . . . 37
5.4.1 Microcontroller . . . 39

5.4.2 Tip Mount Electronics . . . 39
5.4.3 Communications . . . 39
5.4.4 Tip Localization and Position Sensing . . . 40
5.5 Software . . . 40
5.5.1 User Interface for Diagnostics . . . 40
5.5.2 User Interface for End User . . . 40
5.5.3 Control Flow . . . 40
5.6 Final Product . . . 41
5.6.1 Bill of Materials . . . 41
5.6.2 Budget . . . 46
5.6.3 Gantt Chart . . . 46

6 Testing and Validation **47**
6.1 Test Site . . . 47

7 Appendix A - Systems-Level Drawings **48**

8 Appendix B - Sub-System Level Drawings **50**

9 Appendix C - Detailed Drawings **55**

10 Appendix D - MATLAB Scripts **62**

11 Appendix E - SOP **70**

References **73**

1 Executive Summary

Internal inspection of industrial piping systems is a significant engineering challenge. While inspection is critical to determine whether a pipe system is at risk of failure, some pipe systems cannot be inspected due to their challenging geometries.

While many robotic inspection systems exist, they have limited propulsion capabilities because they rely on friction with pipe walls or thrust from propellers. This prevents them from being used in certain pipe systems with vertical pipe segments, tortuous passageways, and unconstrained environments (such as the inside of a large storage tank). The objective of this project is to develop a method for inspecting these inaccessible geometries in a reliable manner. To start, we are focusing on optical inspection of the pipe system shown in Figure 1 which is impossible for current robotics systems to inspect.

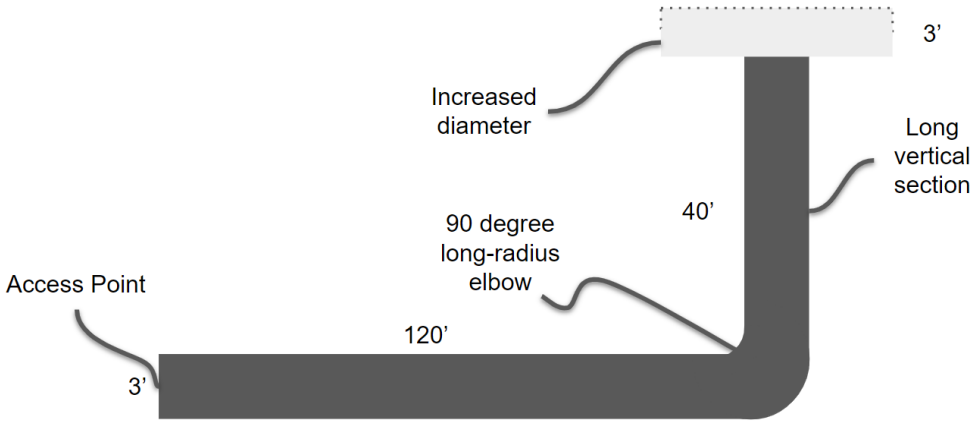

Figure 1: Schematic of the pipe system we are inspecting. Inspection robots enter and exit from the access point.

To inspect the pipe system shown in Figure 1, our team developed a novel version of a soft, continuum robot known as a vine robot. Vine robots are constructed from a thin-walled tube of flexible material inverted into itself, creating an outer body and a length of internal (inverted) material. Vine robots are advantageous because the outer body can be pressurized by a pump outside of the pipe system to generate large propulsion forces at the front of the body. Additionally, the vine robot's pressurized body acts as a structural element, allowing it to be self-supported in free space.

However, the only vine robots built have generally been less than six inches in diameter and twenty feet long, and designed for much simpler research-focused tasks. To create a vine robot for commercial inspection of the pipe system shown in Figure 1, our team needed to first generate novel models of important vine robot operating parameters to inform our design. Next, our team developed numerous subsystems to augment the basic vine robot including a novel airtight mounting platform, novel sensor mount, novel pressure control system, user interface, and standalone electronics control system. Finally, the robustness of our design and accuracy of our models were verified in an on-site test at our sponsor Bechtel's Welding and Applied Technologies Center. We found that...

2 Introduction

2.1 Industrial Pipe Inspection

Existing products in industrial pipe inspection mainly come in the form of borescopes and self-propelled robots, incorporating both tethered and wireless control schemes [1] [2]. Critical product characteristics include reliability, recoverability, image quality, inspection speed, and cost.

2.1.1 Borescopes

Borescopes like the one shown in Figure 2 work by having a user feed a tethered camera through a pipe by hand. Models capable of extending 200ft cost approximately $500 [1], but more sophisticated models with actuated steering can cost upwards of $10,000 [3]. Its manual operation limits its applications in industrial inspection, as it can only traverse straight sections with a few turns or short vertical sections. This is because a boroscope's body must be flexible to bend around turns, but this flexibility prevents an operator from pushing the boroscope forward with significant force.

Figure 2: VEVOR Waterproof Sewer Camera, 200ft.

2.1.2 Inspection Robots

Another approach to pipe inspection is with self-propelled robots. Such robots are either wireless or tethered, and are more expensive with the model in Figure 3 costing $3,600 [2] and a state-of-the-art inspection drone costing $42,000 [4]. Although rovers can navigate complicated sections with many turns, they have difficulties with vertical sections and cannot traverse unconstrained sections. Drones can traverse vertical and unconstrained sections, but have a limited battery life and insufficient propulsion to pull a tether through tortuous pipe systems.

Figure 3: GPK-32 Tracked Wireless Inspection Robot.

2.2 Vine Robots

Vine robots, a recently developed soft, continuum robot, showed significant promise in accessing previously inaccessible pipe systems as demonstrated in search and rescue [5], archaeological [6], and environmental exploration applications [7]. Vine robots are constructed from a thin-walled tube of flexible material inverted into itself, creating an outer body and a length of internal (inverted) material (Figure 4). When the body is pressurized, this internal material is pulled to the tip where it everts and causes the vine robot to grow (lengthen). To retract (shorten) the vine robot, inversion at the tip is achieved by pulling internal material away from the tip towards the base of the robot.

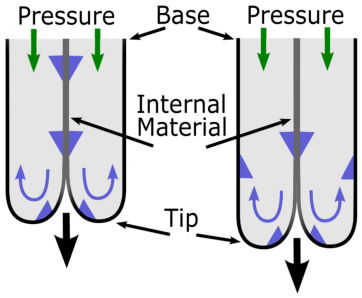

Figure 4: A pressurized vine robot grows as internal material (gray) is pulled to the tip.

Vine robots posses two main advantages over conventional approaches. First, vine robots locomote using pressurized air that can be generated outside of the pipe system. This means a high power air compressor or fan can be used to generate large propulsion forces and locomotion speeds without the vine robot needing to pull the air compressor or fan through the pipe system. Second, as the vine robot grows, its creates an inflated body behind it. If the body is pressurized to an adequate stiffness, the vine robot can grow vertically or in free space [8]. Due to these inherent advantages, vine robot proof-of-concepts in scientific literature, and group members' experience with vine robots the team decided to develop a vine robot for the pipe inspection task shown in Figure 1.

2.2.1 Vine Robot Design

While the infrastructure needed for basic vine robot locomotion is minimal (an air supply and thin-walled flexible tube), for the vine robot to be useful more complicated sub-components are

needed. These have been explored in research applications, most notably in [7], and include:

- Vine robot body: The vine robot body transports the sensors at the tip of the robot, and must be robust enough to withstand the internal pressure, tension when inverted, and environmental hazards. Common vine robot body materials include LDPE (poly tubing) [8], TPU coated ripstop nylon [5], and silicone coated nylon [9]. Optimal material selection is critical due to its effect on robustness, weight, and manufacturability.

- Vine robot tail: The inverted material of the vine robot is often referred to as its "tail". While this can be the same material as the vine robot body, often a string or other material is used. This is because at the vine robots' full length, an equal length of tail is needed to control the vine robot. To reduce weight and complexity, this tail is often a high tensile strength string such as spectra.

- Steering actuators: In situations where controlling the direction of vine robot travel is desired, many types of actuators can be attached to the vine robot body to steer the vine robot. However, steering was not necessary for our vine robot as the path was well defined by the pipe system.

- Base station: In more sophisticated vine robot applications, a base station is used to spool and unspool vine robot body material with motors for storage and length control [5] [6]. These base stations connect to the open end of the vine robot body, and thus must be airtight. Base stations also provide a mounting structure for electronics, communications ports, and air supply ports.

- Air supply: In research environments, pressurized air can be sourced from a large, building-wide system. However, when using vine robots in more challenging environments, an air compressor or fan must be used [6]. For small diameter vine robots which require higher pressures and low flow rates, compressors are used, while large diameter vine robots which need lower pressures and high flow rates use fans. In prior research, passive venting to the atmosphere has been used for retraction as this was sufficient for small diameter vine robots.

- Sensor mount (tip mount): A primary motivation for vine robots have been for cluttered environment exploration, which requires sensors to be mounted to the vine robot. Due to vine robots' unique method of locomotion, sensors cannot simply be statically attached to some point on the vine robot body as it would not move with the vine robot tip. Instead, a sensor mount is used which couples to the vine robot tip and stays there even as material is inverted or everted. Sensor mount development is a challenging, active research area and a significant area of development for our team.

- Retraction device: Though vine robots can be propelled at higher forces than conventional robots, they still encounter the same issues with friction when growing through tortuous pipe systems. This is sometimes occurs because internal material must be dragged backwards through the lengths and turns of pipe to invert the vine robot and retract this. While this can often be overcome through adequate motor torque at the base station, sometimes an additional device is needed at the the tip of the robot to reduce the force needed to retract the vine robot [10]. Based on our analysis we decided that a retraction device added unnecessary complexity.

- Communications system: Based on the application, vine robots have utilized a wide array of communications methods. Sensors can record data to be retrieved after the vine robot is

accessible, but if live data is required, wireless [10] and wired [5] connections have been used such as radio frequency communication, wifi, ethernet cable, and optic fiber.

- Control system and user interface: Complex vine robots can require multiple motors, pressurized chambers, and sensors. Human in the loop control is generally used, with specialized joystick controllers developed for vine robots [6]. Generally a desired speed and direction is specified, and a motorized spool and pressure regulation system are controlled to achieve the desired velocity. Based on the level of complexity and desired ease of use, a user interface can be created to display data and simplify control of the vine robot.

2.3 Inspection Task and Target Specifications

The primary task of this project was the inspection of the 163ft pipe system shown in Figure 1. This pipe system mimics pipe system geometries that currently cannot be inspected in multi-billion dollar construction projects for mining, ports, and chemical transport facilities. This task was given to us by a sponsor of this project, the Bechtel Corporation. As an industrial engineering construction company, Bechtel is primarily concerned with being able to inspect a constructed pipe before handing it over to the end user. Based on discussions with Bechtel's Chief Innovation Officer and on-site Mechanical Superintendent, the following target specifications for our specific task were decided on:

Qualitative Specification	Quantitative Specification
Wired Communications	-
Physically Tethered	-
Live Visual Inspection	-
"Reasonably" Quick	20 minutes to travel entire pipe
Transportable	At least one dimension <36"
	No single component >50lb

Table 1: Target Specifications.

Justification for these specifications and their impact on our design is as follows:

- Wired communications: While our task involves a generic pipe for testing purposes, Bechtel wished for an inspection robot which could transmit data in pipe systems where wireless communications were extremely difficult or impossible. For instance, for a long pipe buried underground with numerous turns. This introduced the added complexity of designing for a cable running along the entire vine robot.

- Physically tethered: A major concern for Bechtel is inspection robots getting stuck in a pipe system. For instance, drones can be very promising for inspection without a tether due to their high maneuverability. However, they have a limited battery life, and if a drone loses power without a tether it is unrecoverable. To prevent this, Bechtel wanted an inspection robots with a tether (which greatly limits robots such as drones due to their minimal propulsion). This requirement had a negligible impact on our design however because vine robots are inherently tethered both through their outer body and internal material.

- Live visual inspection: Bechtel's only sensing requirement was a camera providing live video to the vine robot operator. A simpler data collection method would be to have a camera take a video for the operator to watch after the vine robot traveled through the pipe system.

This would also eliminate the need for wired communications. However, a live video feed allows the operator to focus on specific locations of interest in a more time efficient manner. Additionally, while more complex sensors could be added, it was decided that a camera would be a sufficient proof of concept and capture a significant portion of use cases for inspection robots. No specific resolution, view distance, or viewing angle was given to the team, so best judgement was used to chose between image quality, size, weight, and latency. To allow for a camera to capture any images, a light was also required. Due to the team's lack of experience with pipe inspection optics, on-site feedback from Bechtel engineers was used to determine whether the chosen camera and light were satisfactory.

- "Reasonably" Quick: No specific speed requirement was given our team, but there is a clear trade-off between a fast, complex, and expensive robot; and a slow robot that requires more of an inspector's time. We presented Bechtel with the fastest speed we believed was achievable without significantly increasing the complexity of the vine robot. We estimated this to be 20 minutes to travel the length of the pipe system based on previously achieved vine robot growth and retraction speeds. This condition helped inform our air supply selection but did not otherwise significantly constrain our design.

- Transportable: Bechtel gave to our team two specific constraints on device size. The size limitation is to ensure the device can be moved through a stairwell. The weight limitation is to allow a single worker to transport the device. These limitations proved challenging to meet with our time and budget constraints. However, Bechtel provided the option of splitting the vine robot into multiple components to reduce weight and size. This added some complexity with extra ports and containers needed, but helped us reduce any single component's weight and size

3 Theoretical Modeling

The internal pressure of the vine robot and the corresponding tension in the vine robot tail are important operating parameters [11]. The required pressure is a function of the pipe geometry and inspection requirements, and must be sufficient to prevent the buckling or crushing of the robot body during both growth and retraction. This pressure governs both fan selection and the structural design of the pressurized components. The tail tension governs actuator selection for controlling robot length as the actuator must overcome tail tension to stop or retract the vine robot.

Thus, having a robust model which predicts vine robot operating pressures and tail tensions for various vine robot designs or path geometries is generally useful for design purposes. In particular, the large diameter of the proposed robot makes iterative testing and experimental characterization extremely difficult, increasing the importance of a robust modeling tool. The following discussion presents an overview of the existing models for growth, retraction, and failure modes associated with vine robots that were incorporated into our novel modeling.

3.1 Modeling Pressure and Tension in Growth

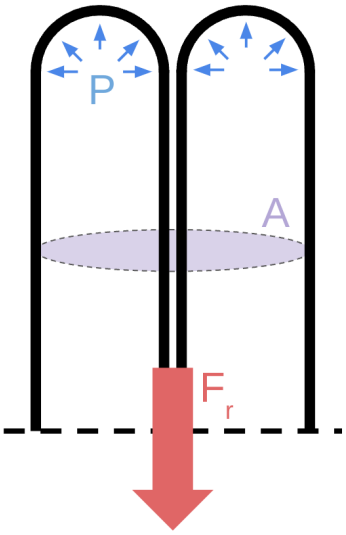

Figure 5: Free-body diagram of the robot tip.

Figure 5 shows a free-body diagram of the tip of a vine robot during growth. The existing analysis for the growth and retraction of a vine robot is based on the empirical observation that the force on the robot's tail due to internal pressure P is $\frac{1}{2}PA$ [12], where A is the cross-sectional area of the robot. From the force balance, the condition for growth is

$$\frac{1}{2}PA > F_r \tag{1}$$

where F_r is the restraining force acting on the robot tip that opposes growth. Blumenschein et. al. [13] show that this restraining force can be decomposed into the following constituent elements:

$$F_r = T_{tail} + F_y + F_v + F_{tip}. \tag{2}$$

F_y is the yield force, not to be confused with elastic yield. This term is a material constant and corresponds to the force needed to deform the material as it is everted through the tip. F_{tip} is a generalized constant term introduced to account for the forces imparted on the robot by the tip mount assembly. This includes the additional friction resulting from the sliding of the tip mount and, in vertical sections, the weight of the tip assembly. Lastly, F_v is a resistive force which increases with vine robot velocity, possibly due to velocity dependent deformation during eversion:

$$F_v = (\frac{1}{\phi}v)^{\frac{1}{n}}A \tag{3}$$

where ϕ and n are empirically determined material properties and v is the robot velocity.

The tail tension, T_{tail} is caused by the tugging of the base-station on the tail and the friction from the tail being dragged along the inside of the vine robot body. Three terms contribute to the tail tension:

$$T_{tail} = \mu_s w L + \sum_i C e^{\frac{\mu_c L_i}{R_i}} + F_{base}. \tag{4}$$

The first term is simply the sliding friction of the tail against the body where w is weight per length, L is the robot length, and μ_s is the coefficient of friction. The second term, described in [9], is known as capstan friction and is caused by the tail sliding against curves in the body due to turns in the path. As above, μ_c is the coefficient of friction, C is an empirical coefficient, L_i is the length of each turn, and r_i is the radius of each turn. As the equation implies, the ratio $\frac{L}{R}$ of the curve makes an exponential contribution to the friction. Moreover, we note that the friction contribution from consecutive turns compound. Lastly, F_{base} is the force exerted on the tail by the base station.

(2) outlines the forces that the internal pressure needs to overcome to cause eversion at the tip. Conversely, the tail tension can be controlled by varying F_{base} to stop the robot from growing at a given internal pressure.

3.2 Modeling Pressure and Tension in Retraction

Retraction can be induced in a vine robot by increasing the tail tension sufficiently. This is formalized by Coad et. al. [12],

$$T_{retract} > \frac{1}{2} P A + F_i + F_v + F_{tip}. \tag{5}$$

where F_i, the inversion force, is the counter-part of the yield force F_y and the remaining terms are identical to (2). $T_{retract}$, the necessary tail tension for retraction, is further decomposed into the following terms:

$$T_{retract} = F_{base} - \mu_s w L - \sum_i C e^{\frac{\mu_c L_i}{R_i}}. \tag{6}$$

Which is a direct counterpart to (4). This equation implies that minimal retraction tension is achieved by reducing the internal pressure. However, there is a lower limit on pressure if retraction without buckling is desired.

3.3 Buckling

When presented with a compressive, axial load, vine robot bodies are susceptible to buckling. As inflated beams, vine robot body stiffness comes from internal pressure, so the potential for buckling is greater than that of a more traditional, rigid robot. For our task of pipe inspection, the possibility of buckling must be considered in finding the minimum required pressure for growth and retraction. Buckling can occur in the constrained or unconstrained sections of the inspection task if the axial loads on the body become sufficiently large, or if a sufficiently large moment is imparted on the body.

The effects of buckling are impacted by the robot body diameter, as a robot body that is the same size as the pipe will have support from the pipe walls to resist buckling, while a smaller robot has reduced stiffness and less support from the walls.

It is known from previous literature [9] that buckling in vine robots can be modeled similarly to buckling in inflated beams, for which prior models have been validated. Principles from these past models were adapted for our specific task to model the conditions under which the vine robot may buckle during operation. Regardless of the mode of buckling, increasing the internal pressure

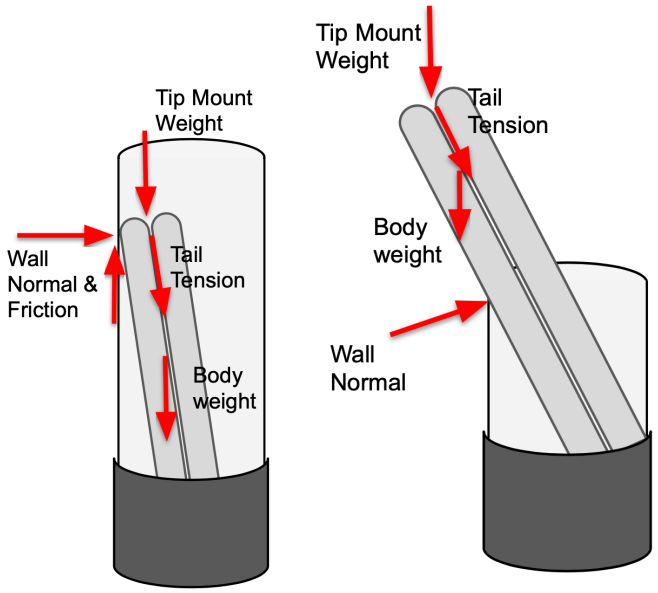

(a) Forces in constrained pipe sections.

(b) Forces in unconstrained operation.

Figure 6: Forces on vine robot body during operation.

of a vine robot or an inflated beam increases the stiffness of the body and improves resistance to buckling. Modeling this allows us to approximate the minimum pressure required to grow or retract without buckling. Three models will be presented for buckling. The first two are derived for constrained and unconstrained sections of the pipe, where the diameter of the robot body is less than that of the pipe. The third model presents crushing, a mode of buckling that can occur when the pipe and robot body share the same diameter.

3.3.1 Constrained Buckling

For our operation, constrained buckling occurs while growing through any of the horizontal or vertical sections, as the robot is constrained by the pipe wall. A diagram of this scenario and the forces on the robot body are depicted in Figure 6.

As described in [14], inflated beams buckle when subjected to an axial force that exceeds a critical value, which we denote F_{cr}:

$$F_{cr} = \frac{EI\frac{\pi^2}{L^2}(P + G\pi Rt)}{EI\frac{\pi^2}{L^2} + P + G\pi Rt} \tag{7}$$

E, I, and G represent the elastic modulus, second moment of area of the body, and shear modulus respectively. P, L, R, and t represent the body pressure, length, radius, and body wall thickness respectively. We sum the components of all the forces acting in the axial direction of the vine robot, and set these equal to F_{cr} to define the critical buckling condition:

$$F_{cr} \leq T_t \cos\alpha + N(\cos\theta - \mu\sin\theta) + mg\sin\theta + m_v g\sin(\theta) \tag{8}$$

where T_t is the tail tension, N is the normal force from the pipe wall, θ is the angle the robot forms with the horizontal, m_v is the mass of the robot body, m is the tip mount mass, α is the angle the

tail tension forms with the axial direction, and μ is the coefficient of friction. If the inequality above is satisfied, then buckling is predicted to occur. While this buckling is not necessarily completely catastrophic, we designed to prevent this due to the complex analysis needed to determine whether this buckling could be tolerated without critical failure.

3.3.2 Unconstrained Buckling

Unconstrained buckling can occur when the vine robot emerges from the 3 foot diameter pipe and grows 3 feet vertically into the unconstrained section. A diagram of this scenario and the forces on the robot body are depicted in Figure 6.

A similar approach to [9] was used, where a moment balance about the point of contact of the vine robot body with the pipe was used to determine the conditions under which the robot will buckle. Rather than a critical axial load that governs whether or not buckling occurs, we consider a restorative moment from the vine robot body pressure that resists the tendency to buckle. This restorative moment is given by PAR, for pressure P, cross-sectional area A, and radius R [12]. Considering the moment imparted by external forces, we find the buckling condition:

$$PAR \leq mg(\frac{d}{2}\sin\theta + L_u\cos\theta) + m_v g(\frac{d}{2}\sin\theta + \frac{L_u}{2}\cos\theta) + T_t(L_u\sin\alpha + \frac{d}{2}\cos\alpha) \tag{9}$$

where L_u is the unconstrained body length and d is the body diameter. Buckling occurs when the inequality above is satisfied.

3.3.3 Crushing

The third mode of buckling considered was crushing of the vine robot body along its central axis. Unlike the previous modes of buckling presented, crushing is not defined by a measure of stiffness, like F_{cr} in (7) or PAR. Instead, crushing occurs simply when the internal pressure of the vine robot is insufficient to support the sum of external forces. The total force supporting the vine robot is the product of pressure and the projected area, PA. If the external forces (including the robot weight) surpass the crushing force, F_{crush}, the vine robot will be crushed by the weight.

$$F_{\text{crush}} = PA \tag{10}$$

3.4 MATLAB Implementation of Theoretical Model

The theoretical modeling was implemented for our targeted inspection task in MATLAB to generate projections of growth pressure and tail tension as functions of vine robot length. This was accomplished by representing the pipe as discrete 0.1' segments and computing the model's output at each segment. The model outputs include the required growth pressure, the required retraction tension, and the required pressure to prevent buckling in both growth and retraction. The MATLAB implementation was abstracted with respect to path and robot geometry, allowing the model to be applied to a wide-range of inspection tasks. This MATLAB script can be found in Section 10.

While the model described above is mathematically simple, the interplay of the forces acting on the tail and the body (see Figure 10) gives rise to several different regimes that needed to be accounted for when implementing the model in MATLAB.

- As the robot starts growing in the horizontal section, the tip, the unspooled, inverted body, and the ethernet cable are dragged in the horizontal section (Figure 10.1).

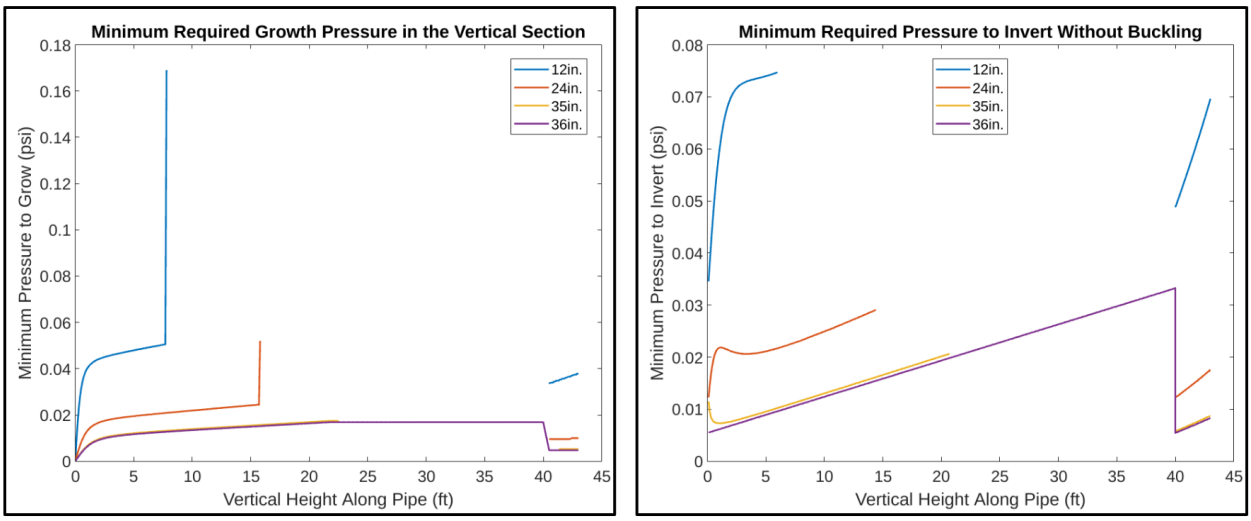

Figure 7: Model predictions highlighting in-feasibility of growth and retraction using small-diameter bodies.

- After the vine robot grows 81.5 feet into the pipe, the body is fully unspooled and the dragged length of the unspooled body is progressively replaced by the tail which has a lower density and coefficient of friction. The ethernet cable is still dragged in the horizontal section (Figure 10.2).
- After 120 feet, the tip enters the vertical section and the weight of the tip mount is added to the tip mount friction. Additionally, the weight of the fraction of the unspooled body that is suspended in the vertical section drags the robot down. However, the tail has not fully replaced the inverted body in the horizontal section and a portion of the body contributes to the sliding friction in the horizontal section (Figure 10.3).
- When the tip reaches 141.5 feet, the tail completely replaces the inverted body in the horizontal section. This regime persists until the robot reaches the end of the trajectory (Figure 10.1).

An important outcome of the MATLAB model, informed by the testing in section 4.2, was determining the optimal robot body diameter for the inspection task at hand. A small-diameter body would be logistically favorable, but a body with a diameter equal to the pipe is stabilized by the pipe wall and leverages friction with the wall to avoid buckling during growth and retraction. Figure 7 highlights the model-predicted growth and retraction pressures for different diameters. The empty sections display it is not possible for the robot to grow and retract without buckling at any pressure based on our model. This result corroborated our empirical evidence and led to the selection of a 36" diameter body.

Sample outputs of the MATLAB model for a 36" body are represented in Figure 8. We observe the change in the trends of required growth and retraction pressure corresponding to the regimes described above. Additionally, note that the maximum operating pressure is estimated at approximately 0.032psi and occurs during growth.

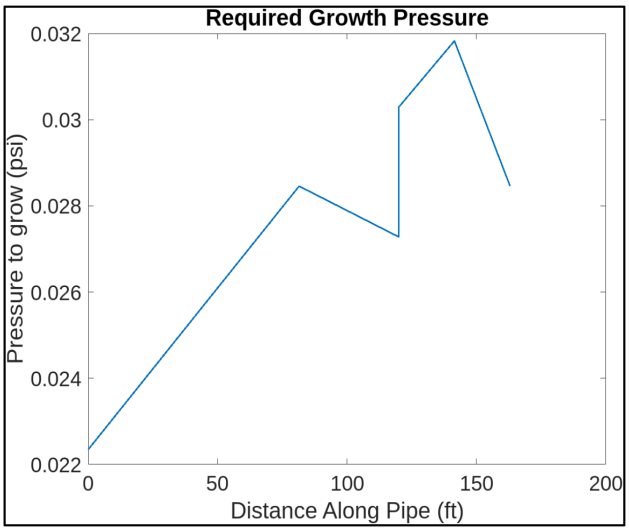

(a) Required pressure during growth.

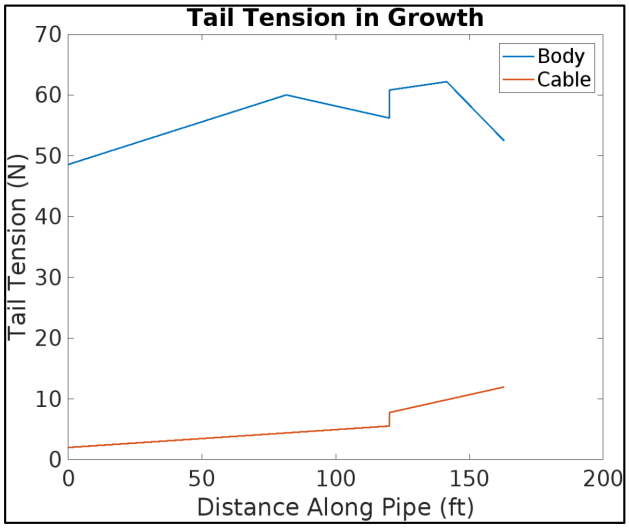

(b) Required tail tension during growth.

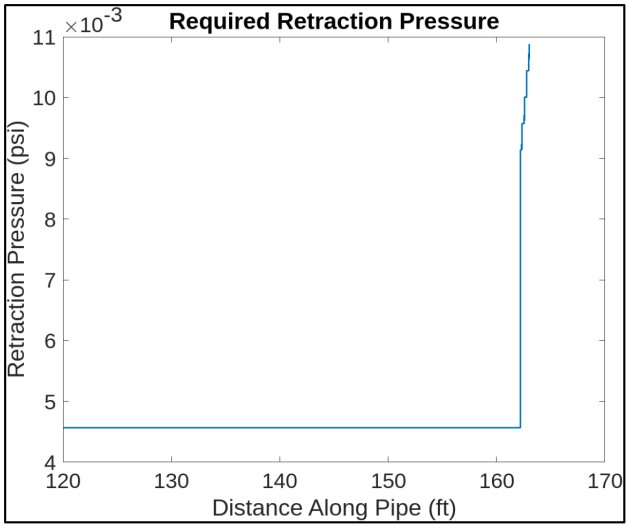

(c) Required pressure for retraction without buckling.

Figure 8: Sample outputs of MATLAB model.

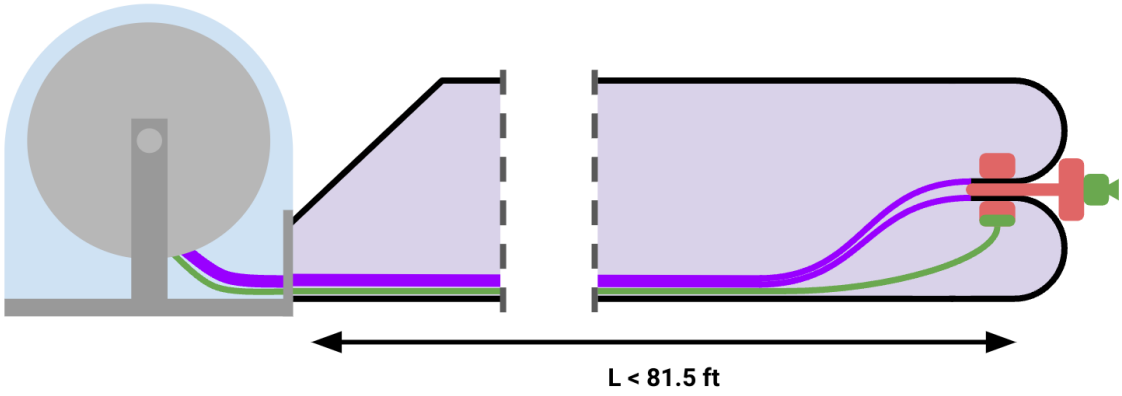
L < 81.5 ft

(a)

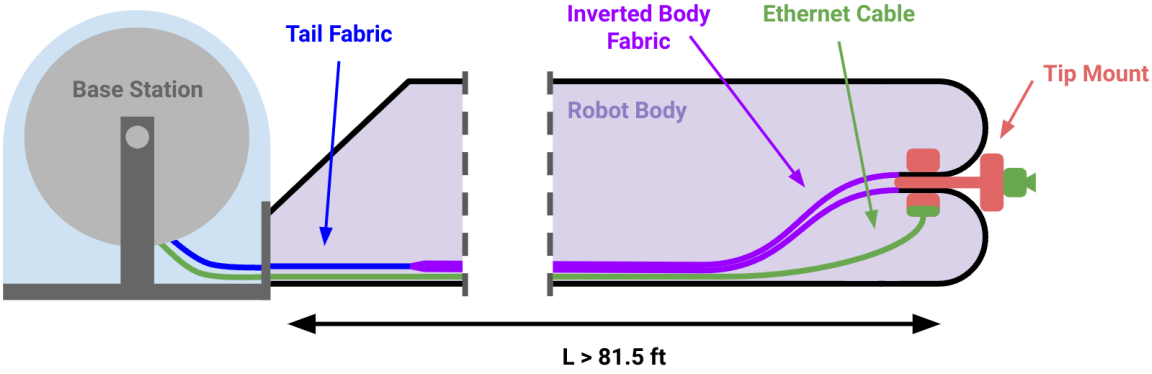
Base Station
Tail Fabric
Inverted Body Fabric
Ethernet Cable
Tip Mount
Robot Body
L > 81.5 ft

(b)

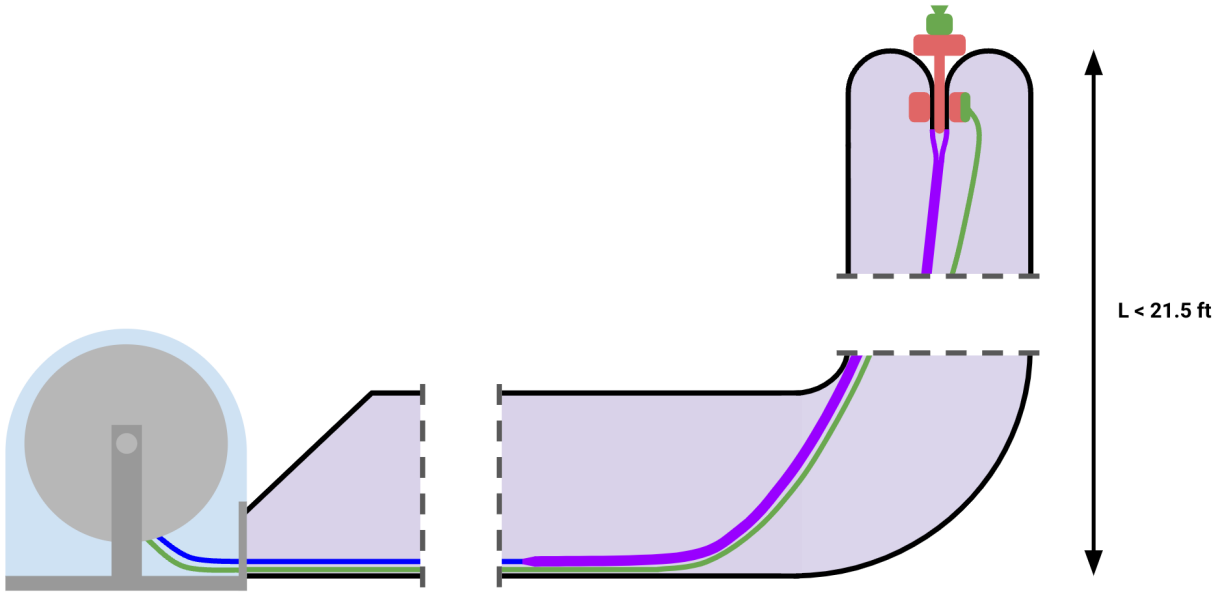

(c)

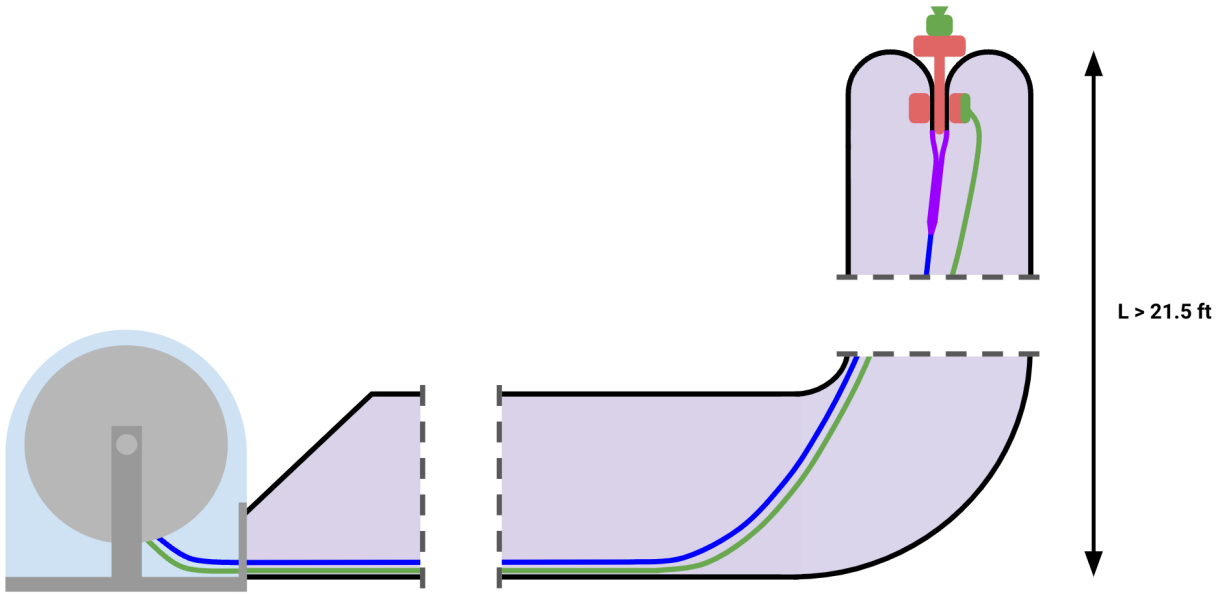

(d)

Figure 10: Continued - illustration of the different operating regimes accounted for in the MATLAB script.

3.5 Failure Modes in Growth and Retraction

The required pressures and tensions generated by the models above can be compared to the failure modes of the robot to determine an operational margin of safety. In particular, two modes of failure are commonly encountered in vine robots:

- **Tensile failure of the tail** occurs when the tail tension supplied by (2) and (5) exceeds the yield strength of the tail fabric. The safety factor for this mode of failure is simply

$$SF_{tensile} = \frac{\sigma_{yield}}{\frac{T_{max}}{A_{tail}}}. \tag{11}$$

- **Burst pressure of the body** is found by treating the body as a cylindrical pressure vessel and finding the pressure that results in yielding.

$$\begin{aligned} SF_{burst} &= \frac{\sigma_{yield}}{\sqrt{\frac{(\sigma_1-\sigma_2)^2+(\sigma_2-\sigma_3)^2+(\sigma_3-\sigma_1)^2}{2}}} \\ &\text{where :} \\ \sigma_1 &= \frac{Pr}{t} \\ \sigma_2 &= \frac{Pr}{2t}. \\ \sigma_3 &= -P. \end{aligned} \tag{12}$$

We note that r is the body radius, P is the body pressure, and t is body thickness. A similar calculation is repeated for the base-station, which is treated as a spherical pressure vessel.

$$\begin{aligned} SF_{burst} &= \frac{\sigma_{yield}}{\sqrt{\frac{(\sigma_1-\sigma_2)^2+(\sigma_2-\sigma_3)^2+(\sigma_3-\sigma_1)^2}{2}}} \\ &\text{where :} \\ \sigma_1 &= \sigma_2 = \frac{Pr}{2t}. \\ \sigma_3 &= -P. \end{aligned} \tag{13}$$

These failure modes were built into the MATLAB scripts to generate the safety factor plots shown in Figure 11. The figures indicate large safety margins (safety factors > 30); this high performance is enabled by a combination of the low required pressure and the high strength of the selected materials. The failure points predicted by the model were empirically validated through burst and tear testing.

3.6 Material Selection

The material the vine robot and tail are constructed from is critical to the performance of the vine robot. First, the vine robot body must be made of an airtight material so the vine robot can be pressurized. Second, the body and tail materials must be robust to external forces including hazards in the environment, internal pressure, and burst pressure. Finally, practical considerations must be

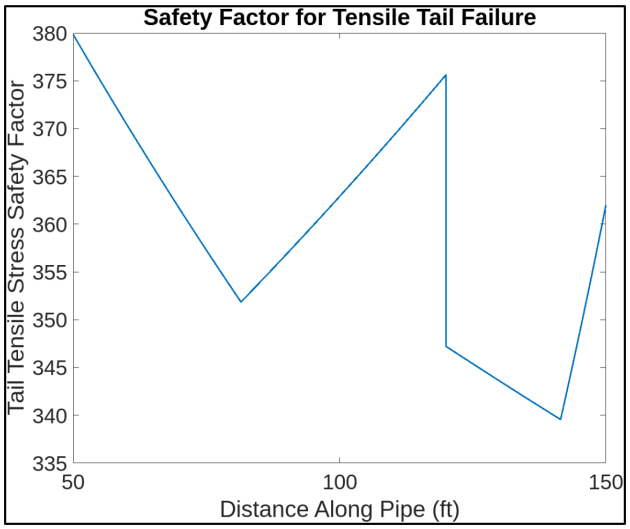

(a) Safety factor with respect to tensile failure.

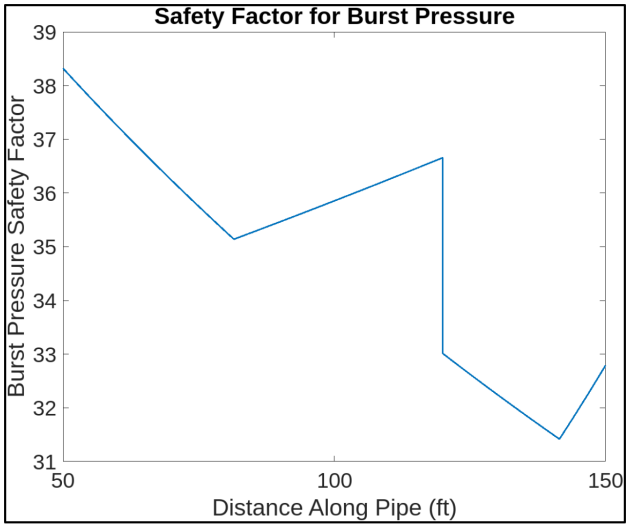

(b) Safety factor with respect to burst pressure.

Figure 11: Sample safety factor plots generated by the MATLAB model.

accounted for including ability to purchase and modify the material into the desired configuration. Given our budget, we only considered materials which would cost less than a few thousand dollars for the full vine robot. Additionally, for our specific task, external steering was not required so the only manufacturability constraint was the ability to form flat sheets and tubes. Assuming these conditions were met, secondary selection parameters included weight, compliance (to simplify the sensor mount design), coefficient of friction, tensile strength, and seal strength. Based on these initial constraints, we conducted broad research and tested three specific materials for the vine robot body:

- PVC (polyvinyl chloride): Manufacturers of pvc bouncy houses and custom rafts were found, which would allow the team to purchase a pre-made tube. This would save significant amounts of manufacturing time versus other materials. PVC can be sealed with adhesives or heat sealed by companies, forming a robust, strong tube. Our team ordered a sample section of tube, but determined that for the desired robustness a PVC tube would be too heavy and stiff.
- Polyether TPU (Thermoplastic polyurethane): As a thermoplastic, TPU could easily heat sealed by our team. TPU prototypes were found to be reasonably compliant, light, and low friction. These prototypes were promising enough that intial characterization testing was completed before comparing the results to silicone coated ripstop nylon.
- Silicone coated ripstop nylon: Ripstop nylon is nylon fabric with a reinforced thread pattern to increase the strength of the fabric and prevent rips from propagating. The silicone coating makes the fabric airtight, and also allows the fabric to be sealed with silicone adhesive. However, sealing with silicone adhesive is a much more time intensive process than heat sealing, and silicone coated fabric cannot be heat sealed. Silicone coated ripstop nylon (colloquially known as "silnylon") is much lighter, more compliant, and has a lower coefficient of friction than TPU as a trade-off. Our team decided that the weight savings, compliance and lower friction of the silnylon outweighed the extra manufacturing time needed, and our final characterization tests and design was completed with this fabric.

Even though silnylon was selected for our vine robot body material, the vine robot tail did not need to be made from the same material because it does not need to be airtight. In order to save weight and thickness (which affects storage volume), a spectrum of fabrics were tested. We decided to use a flat sheet of fabric instead of string previously used in literature for the tail in order to more easily spool the material into a smaller but wider roll as a wide roll was already needed for the vine robot body. Fabric was tested due to its compliance and high specific tensile strength. Tensile tests were conducted on the following fabrics and the results are displayed in Table 2. The optimal fabric was determined to be 0.75oz ripstop nylon.

4 Prototypes and Testing

Several prototypes were created and tested to validate design concepts and inform our final design decisions. Key prototypes included the preliminary base-station prototype, a robot body prototype

4.1 Base Station

Existing vine robot systems feature a base station that serves three primary functions:

- Creates a sealed pressurized chamber around the body to enable pneumatic locomotion.

Fabric	Weight [oz]	Thickness [mm]	12 in. yield tension [N]
0.5 oz Noseeum Mesh (Black)	0.5	0.1	523.854
0.51 oz Dyneema Composite Fabric (Gray)	0.51	0.04	1125.4032
0.56 oz Ripstop Nylon (Orange)	0.56	0.01	557.9928
0.66 oz Taffeta Nylon (Red)	0.66	0.02	1181.9088
0.67 oz Noseeum Mesh (Black)	0.67	0.2	253.098
0.7 oz Ripstop Nylon Mesh (Dark Olive)	0.7	0.08	1252.5408
1.0 oz HyperD (Black)	1.0	0.03	1711.6488
0.75 oz Ripstop Nylon	0.75	0.02	1462.0824

Table 2: Test results for vine robot tail fabrics.

- Carries the body fabric on a spool for transport and ease of locomotion control.
- Serves as a hub for the electrical and pneumatic equipment associated with the robot.

Traditionally, the base station has been implemented as a rigid cylindrical pressure vessel closed-off by two rubber end caps secured with hose clamps. The large scale of the robot developed in this project renders the use of this rigid architecture impractical, particularly when considering accessibility, weight, size, and ease of procurement. Therefore, we explored using a bag to seal the base structure. Our first prototype aimed to examine the viability of this concept by fabricating a mock-up of the base-station for a one-foot diameter robot body. Figure 12 shows the rendering of the prototype design along with an image of the fabricated base-station.

The front rings shown in the rendering are responsible for sealing the robot body to the base-station bag using a series of nuts and bolts. To facilitate this, the techniques detailed in Section 4.4 were used to manufacture adaptive patches from fabric that conformed to the geometry of the sealing rings. The structures were fabricated by laser-cutting thin layers of plywood. Section 4.2 discusses the results of experiments that were conducted using this prototype, but two qualitative observations are noted here; first, the proposed sealing concept proved to be effective in sustaining the pressures associated with large-diameter ($>$ 1ft diameter) vine robots. Second, the structure suffered from poor rigidity which was addressed in future prototypes by using more rigorous structural analysis. Nonetheless, this prototype validated the viability of this alternative base station architecture.

4.2 Experimental Characterization

In addition to acting as a proof-of-concept, the base-station prototype was used to carry out the characterization experiments needed to inform the models presented in Section 3 and guide our

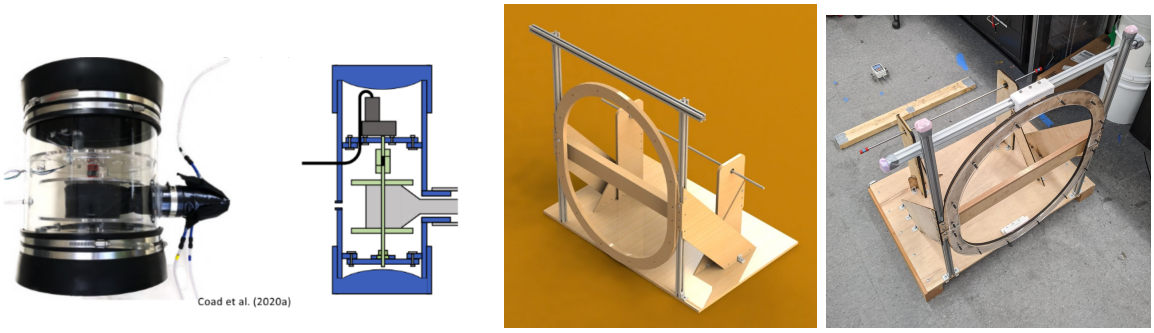

(a) Example of conventional base-station architecture. (b) Rendering of prototype base-station design. (c) Image of the base-station prototype.

Figure 12: Base-station of the vine robot.

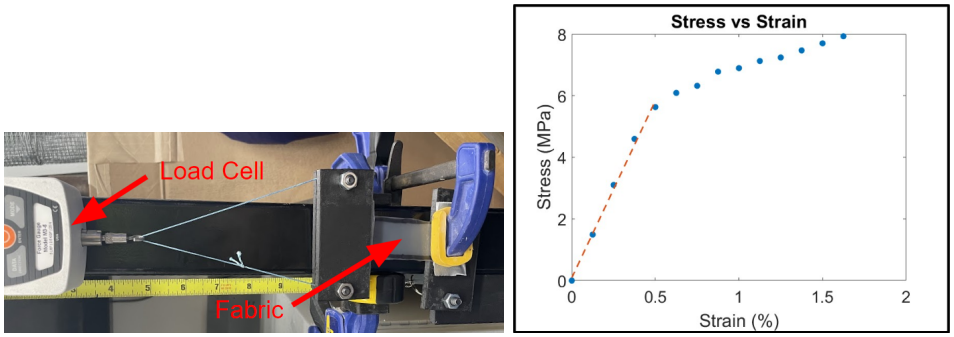

(a) Test setup. (b) Sample stress-strain plot.

Figure 13: Yield stress testing.

final design.

4.2.1 Yield Strength Testing

Empirical stress-strain curves were constructed for the body and tail materials by clamping one end of the fabric in a fixture and pulling on the other end with a load cell. This procedure was recorded in video and load cell readings were correlated with the displacements to estimate the yield strength of the materials. An image of this process along with sample results are presented in Figure 13. A similar procedure was repeated to test the strength of the T-joint used in body fabrication. These tests produced estimates of $\sigma_{yield} = 6.27 \pm 0.5$MPa for the fabric and $\sigma_{yield} = 5.01 \pm 0.07$MPa for the joint.

4.2.2 Growth Testing

Figure 14 highlights the testing setup for growth, retraction and buckling testing with the first prototype. The goal of growth testing was to determine the empirical constants μ_s, F_y, ϕ, and n in (2) and (3) while varying body diameters. Testing was carried out by measuring internal pressure using a pressure sensor and timing the growth of the robot at different lengths; the yield force was obtained from the growth pressure required with no tail length (hence no friction effects). The linear friction factor was obtained by subtracting the yield pressure (as described above) from the required quasi-static growth pressure and comparing the resulting force to the weight of the tail.

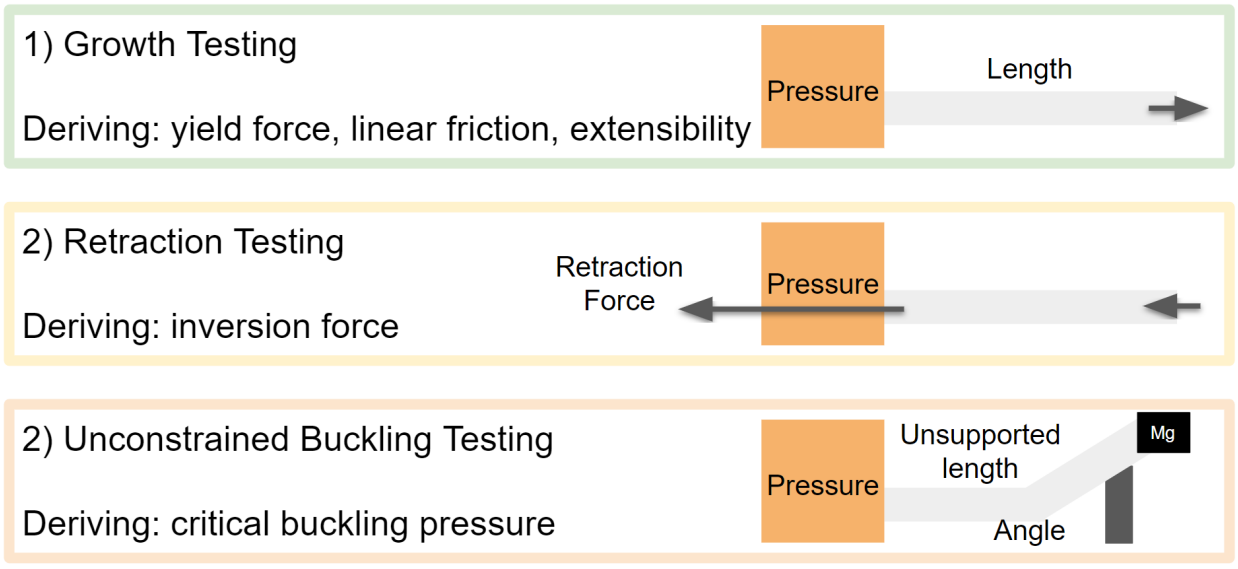

Figure 14: Test setups for growth, retraction, and buckling testing.

The velocity-dependent parameters were found by repeating the experiment at several different speeds and recording the required growth pressure, compensated for yield and linear friction, as a function of velocity. The data points were then curve fitted using the curve fitting tool in MATLAB to match the form of (3).

Sample results from growth testing are presented in Figure 15. As expected, a roughly constant friction factor was obtained and the velocity-dependent parameters closely correspond to the data presented in [13]. Interestingly, the yield force was shown to decrease with diameter, which opposes previous findings. We note that the dominant contributing factor to the required growth pressure was found to be linear friction. These results informed the MATLAB implementation of the theoretical model. Furthermore, the consistency of the results with our anticipated behavior validated the applicability of the existing modeling tools to large-diameter (< 1ft) robot bodies.

Lastly, these tests were augmented with a manual characterization of the capstan friction coefficient which was performed by pulling a piece of fabric around a corner with a load cell while a mass was suspended from the fabric. The mass supplies a known tension at the start of the turn, allowing us to determine the friction factor. We calculated a coefficient of $\mu_c = 0.35 \pm 0.02$ which was used in the MATLAB model.

4.2.3 Retraction Testing

Retraction testing was performed to find the inversion force, F_i, from (5). The test consisted of recording the tail tension T_{tail} with a load cell while monitoring the internal pressure. Figure 16 shows the outcome of these tests; as expected, the inversion force closely corresponds to the yield force. This is because both terms describe the deformation of the material at the tip of the robot during eversion and inversion. We remark that throughout the testing described for prototype one, the spooling of the body fabric was done by manually tensioning the tail.

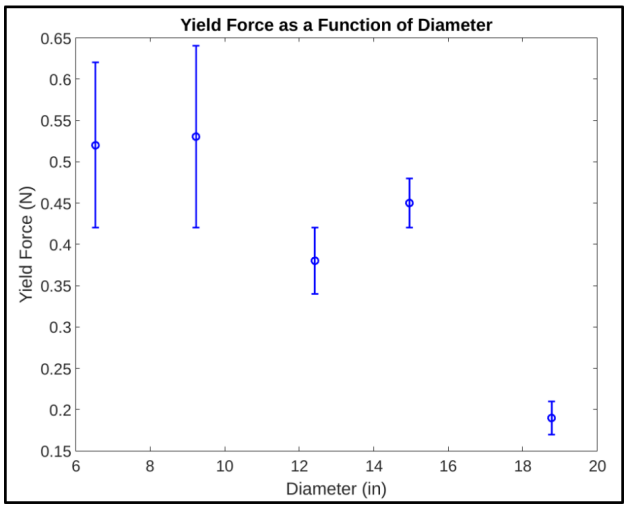

(a) Yield force as a function of body diameter.

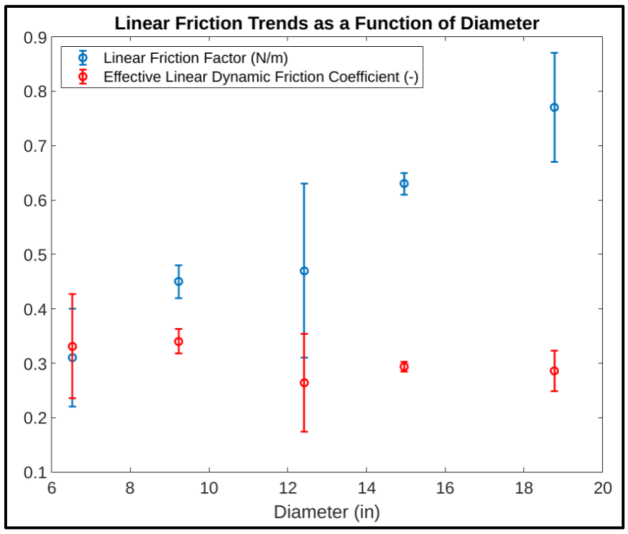

(b) Linear friction as a function of body diameter.

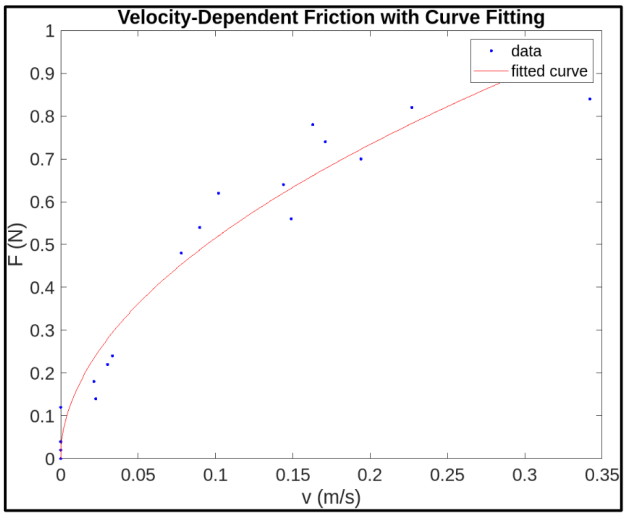

(c) Extensibility force as a function of growth velocity.

Figure 15: Sample results from growth testing with the prototype.

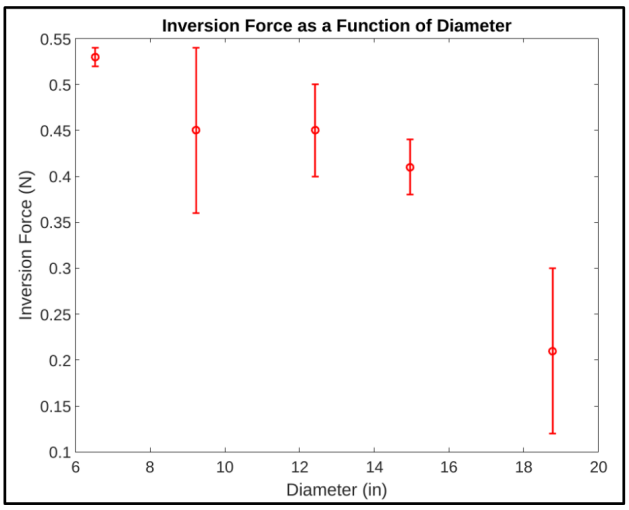

Figure 16: Inversion force as a function of body diameter.

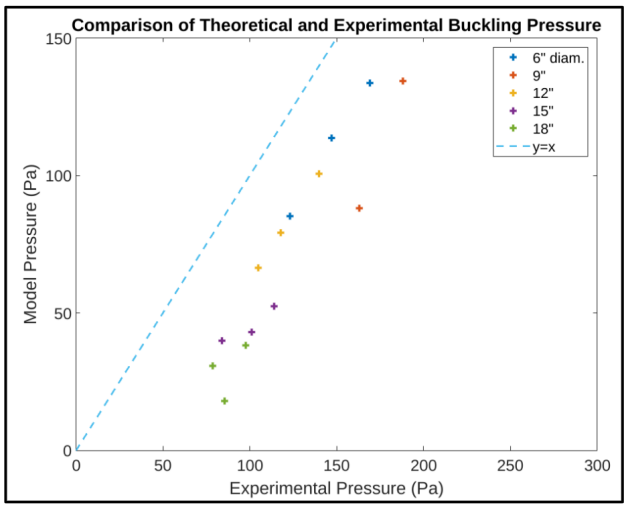

Figure 17: Comparison of theoretical and empirical buckling pressures.

4.2.4 Buckling Testing

The last set of tests with the first base-station aimed to validate our methods for modeling buckling by characterizing the simplest case of buckling - unconstrained buckling as represented in Figure 14. This test was performed by lifting the robot body over a barrier with a tip mass and reducing pressure until buckling was observed. Figure 17 compares the theoretical critical buckling pressure to the observed buckling pressure. It can be seen that the linear trend holds regardless of the selected body diameter. However, there is a permanent offset which, we hypothesize, was caused by an incongruity in the effective cross-sectional area of the robot due to the extremely low buckling pressures. These results were deemed to be a satisfactory validation of our modeling tools for buckling.

h! 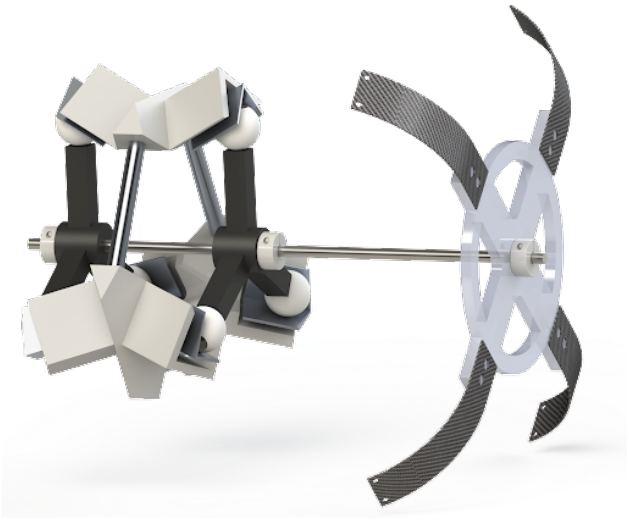

Figure 18: CAD render of a tip mount prototype.

4.3 Tip Mount

Numerous tip mount prototypes at various levels of complexity were created to test different tip mount designs. One of these prototypes is shown in Figure 18. The general requirement for a tip mount is that an outer portion is needed to mount the sensors, while an inner portion is needed to secure the outer portion to the vine robot body and mount communications equipment. Additionally, the outer portion has generally been designed with a large covering known as an umbrella so the vine robot body can propel the tip mount forward. Significant limitations found in the tip mount prototypes have been excessive friction in the interlocking components, compounding bulging in vine robot body, and excessive weight leading to sagging. Further prototype development with testing of multiple new designs aims to rectify these issues. Though tip mounts exist for vine robots, they have only been successfully designed for smaller diameter vine robots which operate at much higher pressures and with much less fabric that must be everted. A successful tip mount will greatly expand vine robot capabilities, but making one requires significant research to develop a stable and robust design.

4.4 Vine Robot Body

The vine robot body uses the silicone-coated 30 Denier Ripstop Nylon (Silnylon). This material was chosen for its strength, air-tight coating, low coefficient of friction, and relative ease to bond using adhesives. Bonding this fabric requires silicone epoxy. The vine robot body fabrication process is as follows:

1. Cut 2 sheets of 60-inch wide Silnylon sheet to desired length (163 ft)

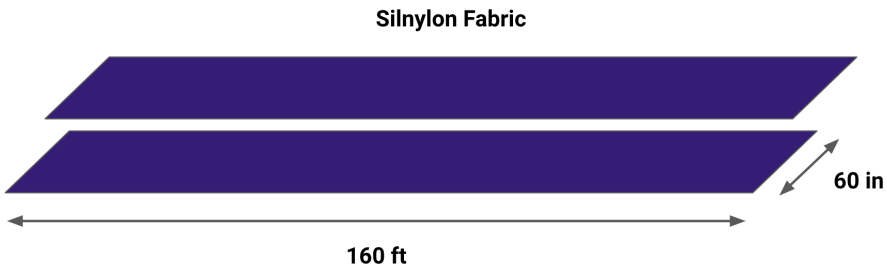

2. Lay silicone epoxy along the length-wise edge of one sheet of Silnylon

Note: Bonding was completed in 2 passes, we first laid down a series of silicone epoxy beads (1 ft apart) to initially secure the two sheets together. We then deposited a continuous line of epoxy along the edge for bonding

3. Lay the edge of the second sheet atop the silicone-epoxy-coated edge of the first sheet to form a lap joint, apply pressure and wait for the adhesive to cure

Note: This procedure was done in segments of approximately 3 ft given the assemblers' limited ability to manipulate large sheets of fabric and apply pressure over large distances

4. Fold the jointed sheet along the bonded edge and repeat steps 2 and 3 for the remaining 2 long edges to form a Silnylon fabric tube

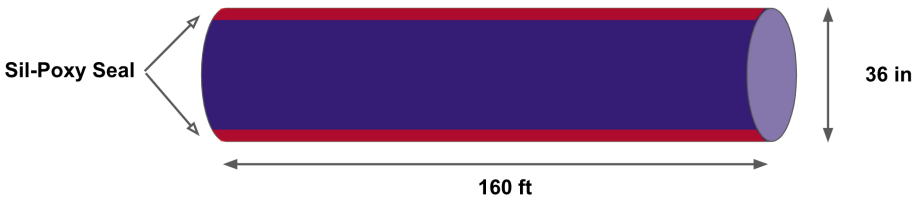

This method for fabrication is straightforward and repeatable. Two 60-inch-wide Silnylon sheets had to be bonded because suppliers do not offer 120-inch-wide spools of Silnylon. For large-scale

h!

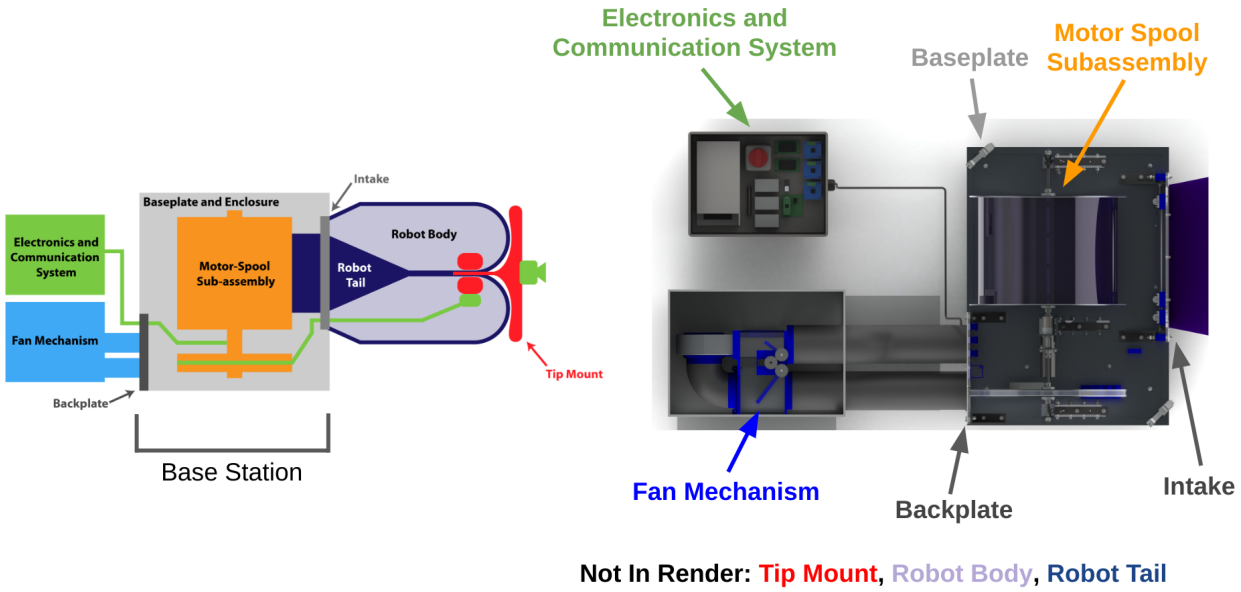

Figure 19: Schematic breakdown of the sub-assemblies in the final design.

vine robot applications, silicone-based adhesives allow for the robust bonding of large sheets of fabric to form the tubular shape of the robot body.

An 80-feet long prototype vine robot body was fabricated and inflated to test for leaks. By closely examining the inflated body along the seams (both visually and acoustically), we discovered no apparent leaks caused by the fabrication process. The success of this initial prototype led us to use this fabrication prototype for the final iteration of the robot.

5 Final Design

The final design, informed by the prototyping and testing described above, features a 36" diameter robot body that grows from a rigid base-station sealed with a compliant bag. The proposed robot relies on a new tip mount design for carrying sensing equipment. Modular fan mechanism and electronics assemblies support the operation of the base-station while adhering to the required single-component size limits. The detailed design of each assembly, abstracted in Figure 19, is presented in the following section.

5.1 Base Station v.2

The base-station consists of the baseplate, the spool-motor assembly, the intake assembly, and the backplate assembly (Figure 19) It contains the majority of the rigid structural components of the robot.

5.1.1 Spool-motor Assembly

In order to store and release the vine robot body, vine robot tail, and ethernet cable in an organized manner, a spool-motor assembly was designed to reel both of these components, as shown in Figure 21. Both of these spools consist of rods supported by U-Channels, spool plates that constrain the

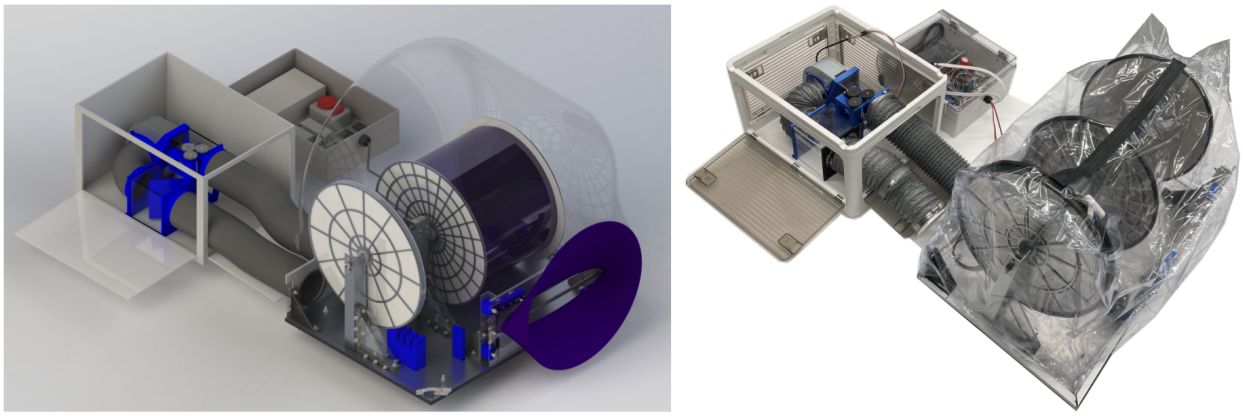

Figure 20: SolidWorks rendering of the base-station along with an image of the finished assembly.

spooled material, and brackets that hold the U-Channels and provide stability. The rods are attached to motors that actuate the spooling and unspooling processes. The fabric spool has an additional clamp mechanism that clamps the fabric to the spool using shaft collars.

U-Channels were selected because of their convenience in fabrication as well as their rigidity. Holes were machined along the U-Channels to attach bearing blocks. All machining work was completed in-house using CNC equipment to meet the imposed tolerances on the critical features. The U-Channels, in particular, were toleranced tightly due to the importance of avoiding eccentric loading of the shafts.

The brackets are composed of 3D printed pieces and laser-cut, acrylic components. The 3D printed pieces are L-shaped so that screws can be used to mount the brackets to both the base plate and the vertical U-Channels. Acrylic triangles are also attached to improve the rigidity and provide more support. These brackets allow for precise mounting of the U-Channels and provide the strength required to hold the spools in place during operation.

The circular spool plates constrain the spooling of the fabric and ethernet cables so they spool in an organized manner. These plates are constructed of solid aluminum plates glued to ribs that add rigidity without unnecessary weight.

5.1.2 Motor Selection

In the most common vine robot architecture, a motor is responsible for the spooling and unspooling of the robot body. A motor was also determined to be the optimal actuator based on its continuous output and high power density. In our application, the existence of a secondary Ethernet-cable spool necessitates the use of a second motor. The need for high-torque, medium-speed continuous rotation makes DC motors a natural candidate for this task. Specifically, brush-less DC motors were utilized due to their low cost and ease of controllability.

The motors were selected to match the torque, speed, and power requirements of the spool's in order to meet the 20-minute deployment benchmark. The tension acting on the spools was estimated by our modeling in Section 3; The spool diameter was then empirically characterized and extrapolated using an 80-ft test body. Knowing both the applied tension and the lever-arm of the spool allows us to estimate all parameters of interest:

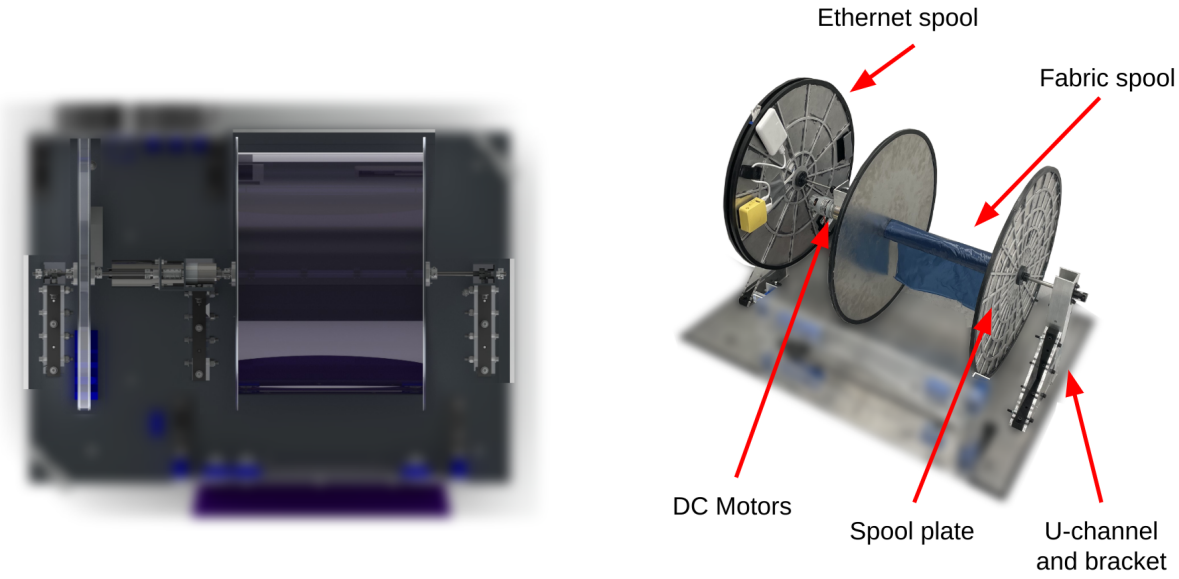

Figure 21: SolidWorks rendering of the spool-motor assembly along with an image of the finished prototype.

$$\begin{aligned} \tau &= T_{tail} \cdot r_{spool} \\ \omega &= \frac{2 \cdot v}{r_{spool}} \\ P &= \tau \cdot \omega \end{aligned} \tag{14}$$

Note that linear velocity is multiplied by two because the tail velocity is double that of the robot velocity [11]. Figure 22 highlights a numerical evaluation of the required performance metrics for the motors. We observe that the torque required for the fabric spool motors is much larger due to the substantial friction acting on the body. The motors presented in Table 3 meet these requirements with a safety factor of 2 or more and were selected for the final prototype.

Supplier	Rated Torque (Nm)	Speed (RPM)	Power (W)	Gear Ratio
ISL International (via Digikey)	32.5	10	33.5	500:1
Polulu	2.26	200	10	50:1

Table 3: Specification of chosen DC motors.

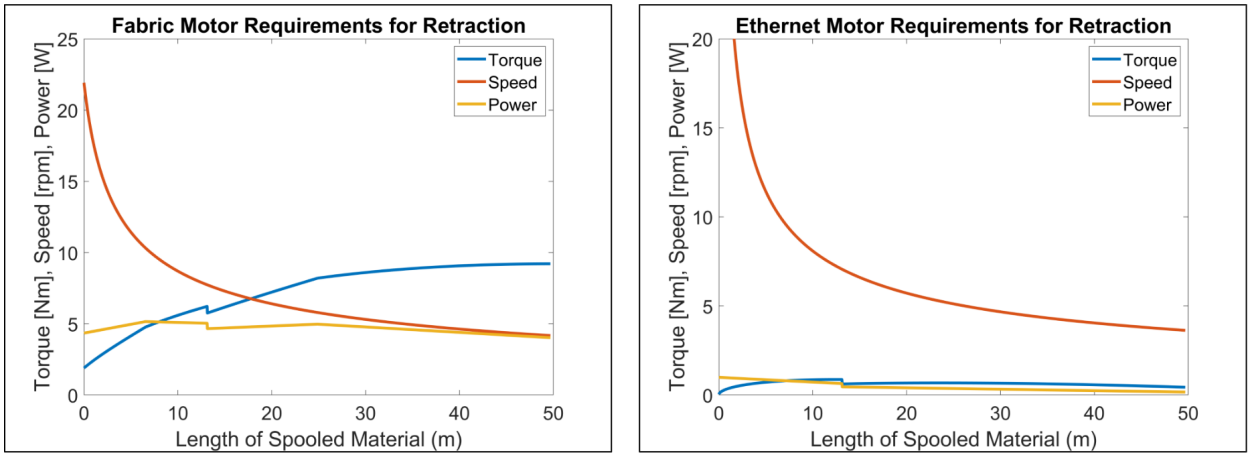

Figure 22: MATLAB-generated motor requirements.

5.1.3 Bag Sealing Method

An airtight seal is necessary for the growth of the vine robot. The method of sealing that was selected is a U-Channel clamp system. The edges of the baseplate are lined with rubber, a custom vinyl bag is oriented to envelop the base station, and the U-Channels are pushed against the bag and rubber strips. Finally, clamps between the U-Channels are engaged to squeeze them together and press the vinyl bag into the base plate. This method offers a simple to adapt, off-the-shelf solution to sealing that performs adequately. For ease of access, an airtight zipper was added to the top of the vinyl bag.

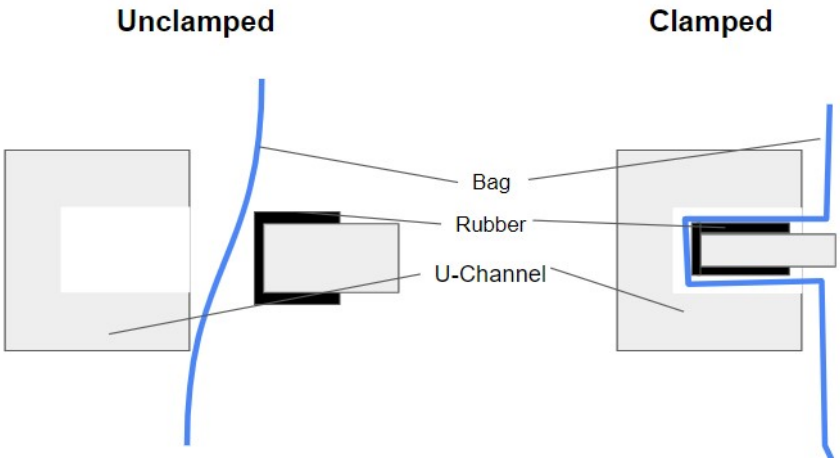

Figure 23: Side View Visualization of Clamping Mechanism

5.1.4 Intake Plate Assembly

In order to seal the vine robot body to the base station while allowing for the fabric and Ethernet to unspool through the interior of the vine robot, an intake plate was designed, shown in Figure 24. The intake plate assembly consists of rollers that guide the fabric and Ethernet cables to and from their respective spools. Bearings for these rollers are held using 3D printed blocks. The intake plate is also composed of two identical acrylic plates that screw together and clamp the robot body fabric and the base station bag together. This clamp creates an airtight interface between the robot body and the base station bag.

5.1.5 Back-plate Assembly

The back-plate interfaces with both the electronic box and the fan mechanism. Two acrylic plates clamp the bag onto mounting brackets bolted to the base plate (Figure 25).

Two Molex connectors and a 9-pin connector are secured in 3D printed holders and epoxied to the inner acrylic plate. Vents from the fan mechanism interface with the backplate with a pair of vent coupling.

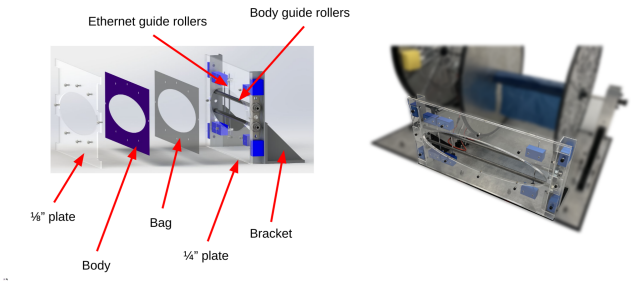

Figure 24: SolidWorks rendering of the intake plate assembly along with an image of the finished prototype.

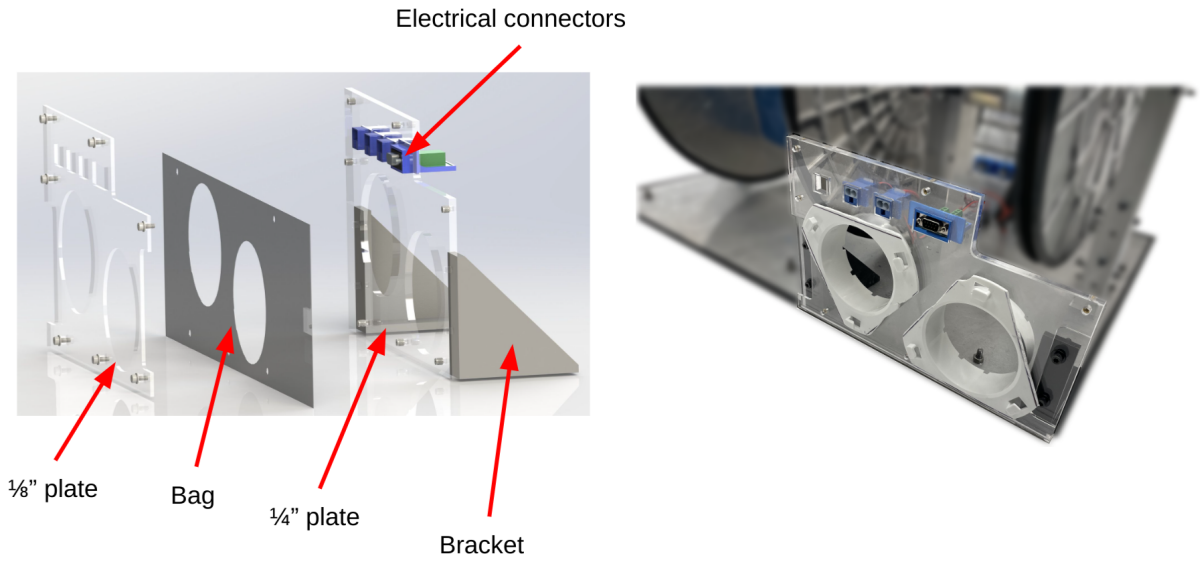

Figure 25: SolidWorks rendering of the back-plate assembly along with the finished prototype.

5.1.6 Ethernet Cable Routing Assembly

As discussed previously, the Ethernet cable is spooled up on a separate reel that is located next to the fabric spool. As a result, the cable needs to be rotated 90 degrees and re-routed laterally before passing through the intake assembly. The Ethernet cable routing assembly, seen at the base of the Ethernet spool in Figure 20 achieves this by guiding the cable through a series of ball bearings that progressively change the orientation and lateral position of the cable.

The assembly consists of two 3D printed blocks that host 5 pairs of ball bearings. One bearing from each pair is fitted with a guide structure that encapsulates the cable and ensures that the cable only comes in contact with rolling elements. The shaft holding the bearing is press fit into the 3D printed housing to eliminate fasteners and additional design complexity; this also allows the bearings to be removed to insert the ethernet cable.

5.1.7 Baseplate

All of the base-station sub-assemblies described above are fixed to the baseplate which acts as an anchoring feature. The plate is fabricated from 1/8" thick 6063 aluminum to achieve reasonable stiffness without exceeding the imposed weight limit.

5.1.8 Simulation-Based Optimization

The design of all of the structural components in the above sub-assemblies was aided by Finite Element Analysis (FEA) simulations. Selected results from these simulations are presented in Figure 27. The solid-static simulations were set up in the following manner: for any given structural component, the grounding feature was geometrically fixed, and a uniformly distributed load, obtained from the theoretical model, was applied. The ultimate objective of these simulations was to study two phenomena:

- **Yield**: The maximum stress in each component was compared to the yield strength of that component. A safety factor larger than 2 was required for all structural components.

- **Displacement**: The maximum linear displacement in the components interfacing with the shafts was limited to 1.0mm.

Both of these benchmarks were selected arbitrarily based on the engineering judgment of the designers. It is important to keep in mind the approximate nature of the results of these simulations; the loading and constraint conditions in the simulations are greatly simplified and bolted surfaces were assumed to be bonded due to the use of several highly pre-tensioned bolts. Rather than gaining an exact understanding of the failure condition, the goal of the simulation studies was to obtain a rough estimate of the strength of the assemblies for preliminary proof of concept.

Lastly, the structural simulations were paired with hand calculations when necessary. Importantly, the strength of each shaft was assessed analytically due to their critical function, and the hand calculations matched the maximum predicted stress, within 5% accuracy. Additionally, hand calculations were performed to examine the fast fracture of the acrylic plates. These calculations indicated that fast fracture would not occur before substantial yielding in the supporting structure.

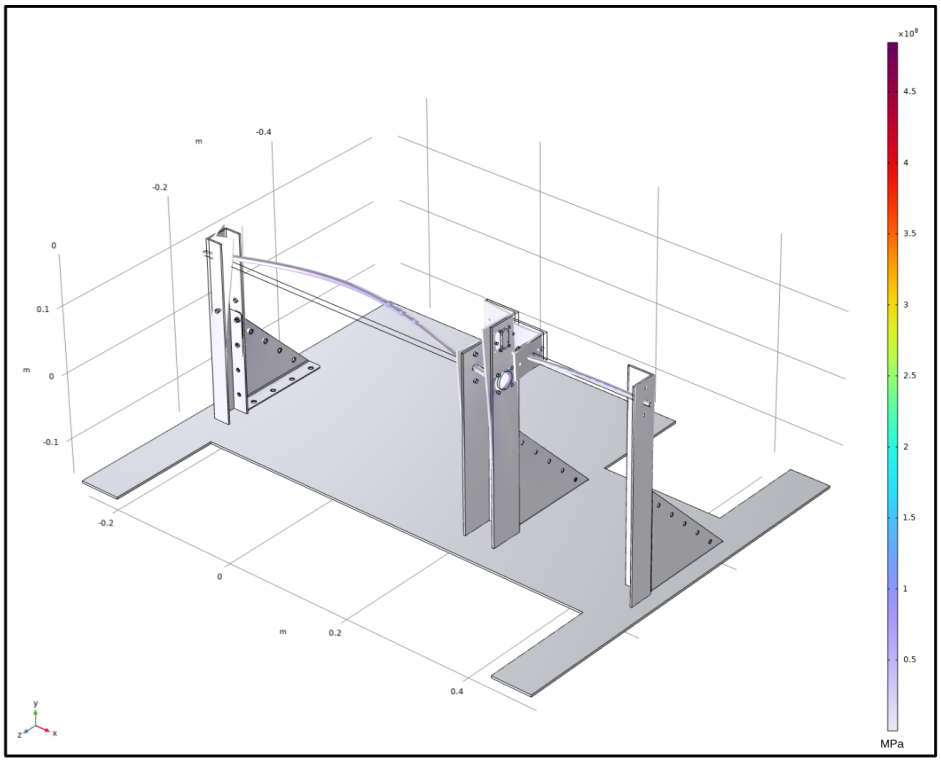

(a) Spool-motor assembly.

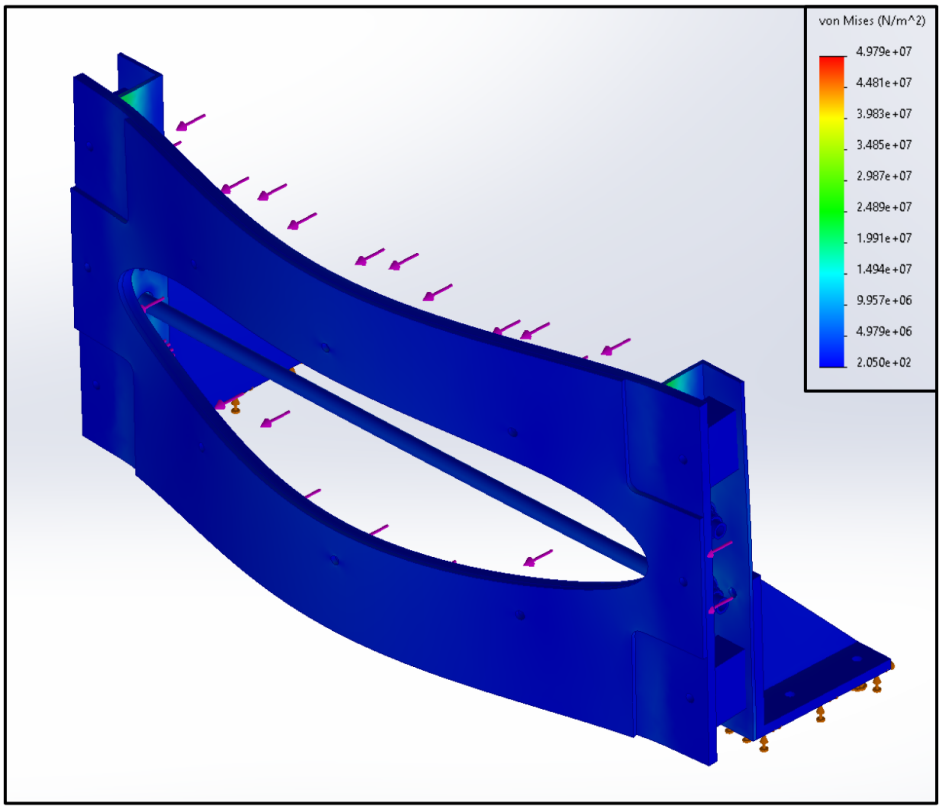

(b) Intake assembly.

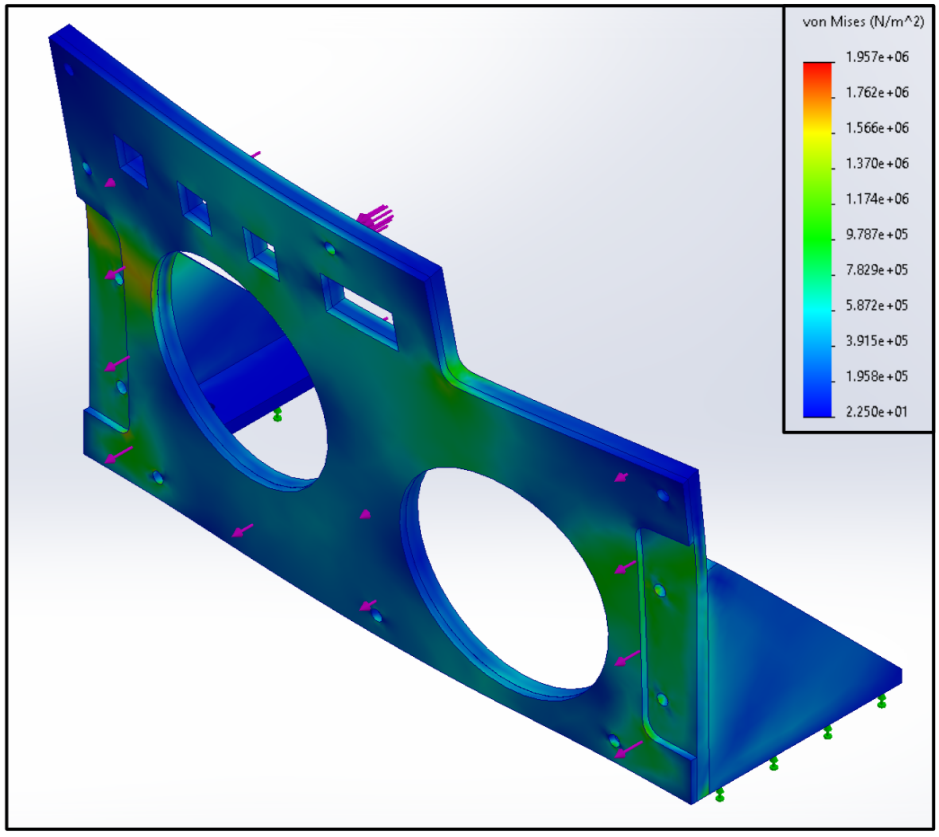

(c) Backplate assembly.

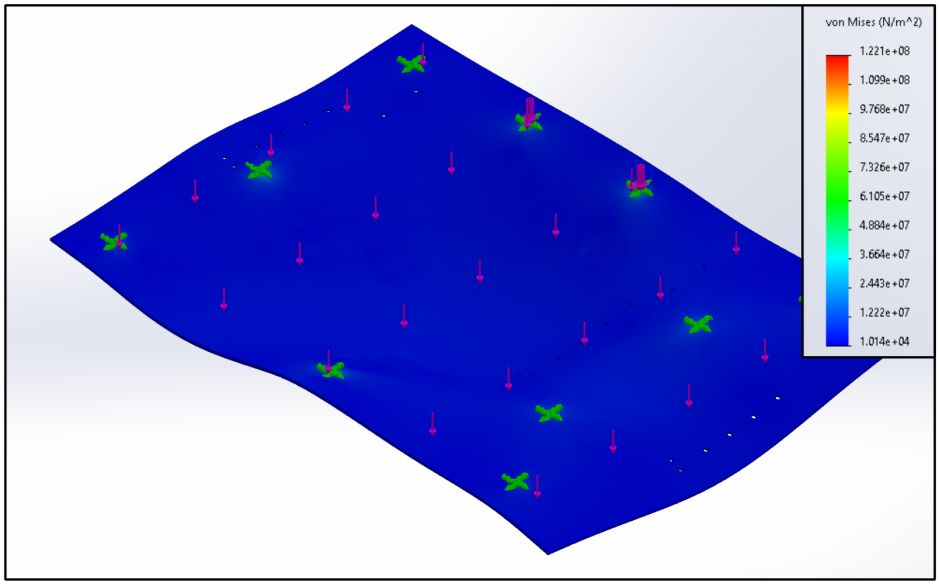

(d) Baseplate.

Figure 27: Sample results from FEA analysis on the critical structural components. The base of the structures was geometrically fixed, and uniformly distributed loads obtained from the theoretical model were applied to obtain these Von-Mises stress plots.

5.2 Tip Mount v.3

TBD Due to the extreme complexity and novel nature of a vine robot tip mount at this scale, tip mount design is still in prototyping and development.

5.3 Fan Selection

In order to inflate the vine robot body through the entire pipe in a reasonable amount of time, a fan with suitable specifications was sought. To find the maximum operating pressure and flow rate, the model described in Section 3 was used to find the maximum growth and retraction pressures required to traverse the 160-foot-long pipe in 20 minutes.

In the most tortuous section of the pipe, as the vine robot grows at maximum speed, our model indicates a maximum internal pressure of 0.035 psi. The required growth pressure along the pipe, according to our model, is shown in Figure 8. Given the desired speed to grow 160 feet in 20 minutes, for a 3-foot diameter robot, the desired flow rate can be found to be 56.5 cfm (cubic feet per minute):

$$Q = V \cdot A = \frac{160 \text{ ft}}{20 \text{ min}} \frac{\pi(3 \text{ ft})^2}{4} = 56.5 \frac{\text{ft}^3}{\text{min}} \tag{15}$$

The selected fan will also be used in the case of retraction, because the body pressure alone is not sufficient to expel air at the desired flow rate. The desired rate of retraction is the same as the desired rate of growth, so the flow rate is also 56.5 cfm. However, the operating pressure in retraction is 0 psi because the air is moved from high pressure in the robot body to atmospheric pressure.

For this application, centrifugal fans were the most optimal design, as they offered the correct range of pressure and flow rate in a small form factor. The fan that was ultimately selected was the Pelonis RB1881, shown in Figure 28. This figure also shows the operating curve, which indicates a flow rate of approximately 100 cfm at our maximum pressure. This provides a safety factor of 1.8 over our desired flow rate of 56.5 cfm in growth, and a safety factor of 2.3 in retraction. Another advantage of this fan is that it allows for PWM control of the rotational speed, which allows for more fine-tuned control of the flow rate it provides.

5.3.1 Fan Intake Mechanism

Centrifugal fans cannot be run in reverse, so in order to use the selected fan in both growth and retraction, an intake mechanism was designed to allow for switching the direction of flow. The intake mechanism uses a servo motor and a 3-gear configuration to actuate doors that redirect the flow depending on the operation of the vine robot. The design is shown in Figure 29. The corrugated, flexible tubing that leads out of the fan box interfaces with the base station back plate, and the two acrylic chambers have openings that allow for air to enter the inlet or to leave from the outlet at atmospheric pressure. The actuated doors will either close or open the openings to the environment, while simultaneously opening or closing the interfaces to the vine robot interior. Switching the fan mode of operation is depicted in Figure 30.

5.4 Electronics

In order to read sensor data and send commands to the actuators, an electronics control system was designed. The microcontroller, communication system, and tip mount electronics will be outlined in the following subsections.

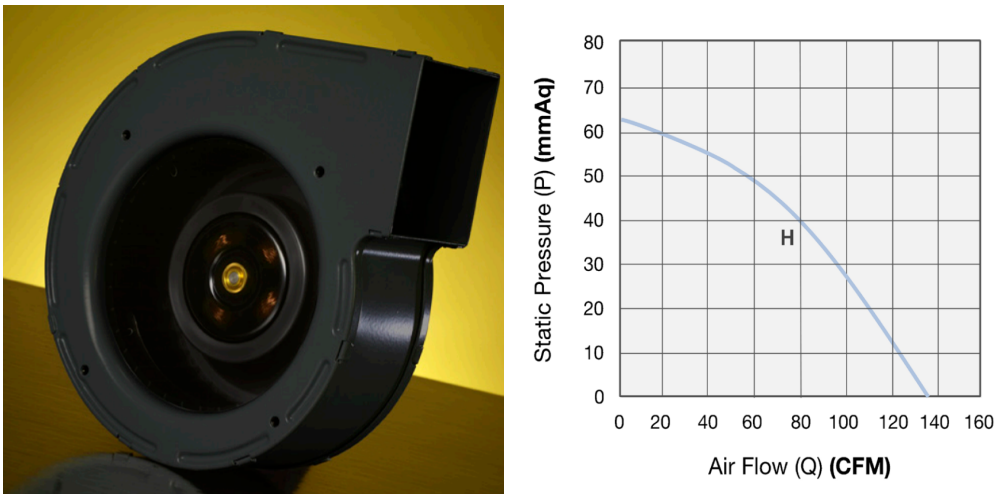

Figure 28: Pelonis RB1881 centrifugal fan (left). Operating curve shows flow rate of approximately 100 cfm at 0.035 psi (24.6 mmAq) (right).

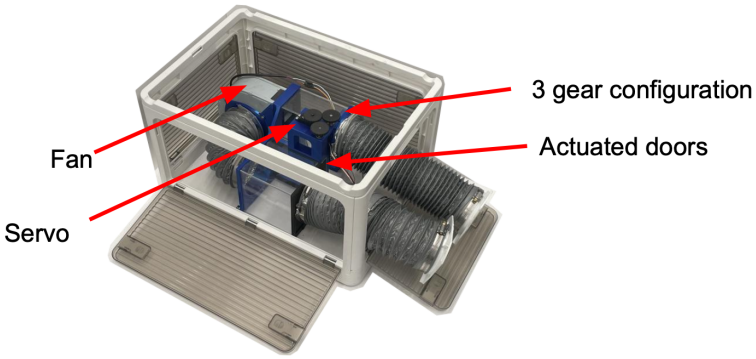

Figure 29: The fan intake mechanism relies on a 3-gear configuration, actuated by a servo motor that rotates doors to redirect the flow of air in or out of the robot body.

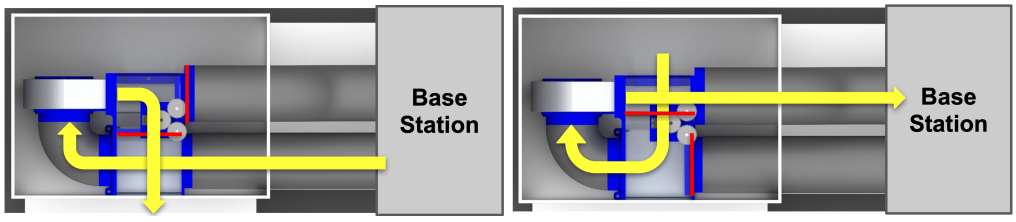

Figure 30: The fan will switch between the retraction (left) and growth (right) configurations via the fan mechanism. Yellow lines indicate direction of airflow and red lines depict doors over the 2 acrylic chambers that redirect the direction of flow. Yellow lines of flow that pass under or over each other indicate when the flow of air travels around one of the acrylic chambers and enters or exits the intake mechanism.

5.4.1 Microcontroller

The electronics control system uses the Raspberry Pi Pico W (RPI Pico) to control all motors and process sensor data. This controller is chosen based on its WiFi capabilities as well as ease of use. The python implementation allows for real-time command line testing, which alternative controllers, such as Arduino and ESP32, do not support given their C framework.

5.4.2 Tip Mount Electronics

In order to inspect the pipe during operation in real-time, Bechtel requires the robot tip camera to have clear visuals at low latency. We determined that a resolution of 1080p and a lag below 500 ms are adequate for our applications.

The camera system at the tip consists of a USB webcam that connects to a Linux microcomputer (Orange Pi Zero 2). The microcomputer will connect to WiFi and run the *virtualhere* software to broadcast USB signals across the local network. The USB webcam is a standard 1080p 60 fps webcam. The Orange Pi Zero 2 was chosen based on its compact size and processing power to handle wireless broadcasting of the USB signal from the webcam. This system operates with an average latency of 200 ms.

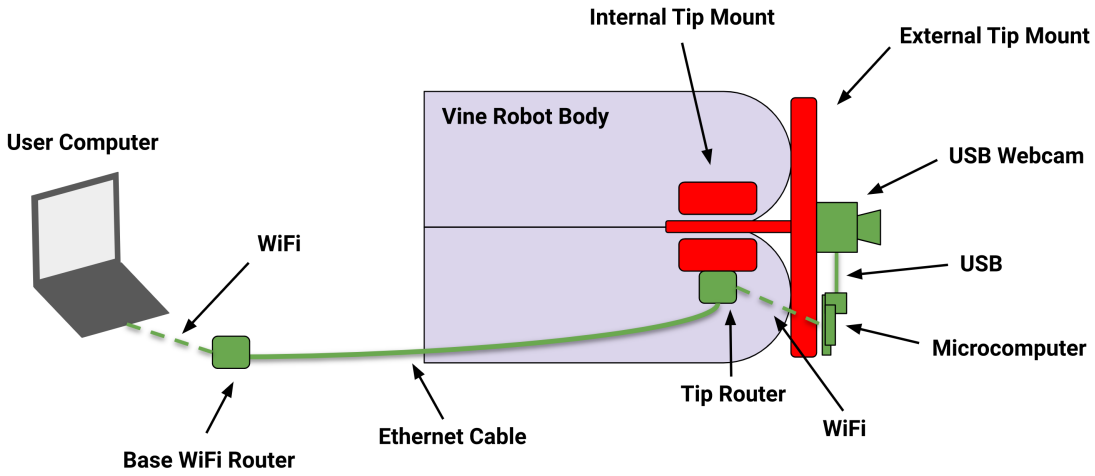

Figure 31: Robot tip communication schematic. Internal and external tip mount components are separated by the vine robot body so we employed a wired-wireless hybrid approach to transmitting video data from the tip

5.4.3 Communications

A WiFi router at the base station hosts a local wireless network through which the user can communicate with the RPI Pico and send commands. The network is also extended to the tip of the robot through a spool of Ethernet cable and an extender router mounted on the interior of the tip mount. This method satisfies Bechtel's requirement for using a primarily wired connection from the base to the camera at the tip.

The core constraint of our system comes from how the inner and outer tip mount components are separated by the robot body fabric. As the robot grows, the fabric would slide past the tip mount, meaning that we cannot pass a wired connection directly from the tip camera back to the base-station.

The high-level communication scheme (Figure. 31) mixes both wired and wireless connections to overcome the imposed constraints. A wireless camera at the tip will connect to the network of the WiFi router (serving as a signal repeater) at the tip, which extends the network from the base WiFi router using an Ethernet cable.

5.4.4 Tip Localization and Position Sensing

TBD - Describe sensing method to track the position and velocity of the tip

5.5 Software

In order to use the vine robot for inspection, a user interface (UI) was created for the user to conveniently view the sensor readings and the live camera feed. In addition, this interface allows the user to send wireless command signals to the various actuators on the vine robot to control its operation.

5.5.1 User Interface for Diagnostics

In order to test the various actuators and sensors that interface with the Raspberry Pi, the UI shown in Figure 32 was designed. This version of the UI allows the user to control the fabric spool (motor 1), ethernet spool (motor 2), brake mechanism, fan rotational speed, and the fan intake servo motors. For these components, sliders were used to allow for intuitive control over the PWM (pulse width modulation) signals for motor speed commands. Value entry elements were added to also allow the user to specify exact PWM or voltage commands. Live readings of the pressure sensor and the feed from the camera are displayed continuously once the buttons to begin streaming them are pressed.

The interface was designed using Python and the PyQT module. Python was selected for this application because of our integration of the sensors with Raspberry Pi and for ease of use. The PyQT package was selected because of its performance in relaying the live camera feed and for its library of convenient UI elements.

5.5.2 User Interface for End User

For the end user, we intend to design a user interface similar to the one designed for diagnostics testing, but to abstract the low-level controls into higher-level commands. This user interface would allow the end user to have simple controls to change the direction of growth/retraction and speed of the tip. The user interface will take these commands and from them, determine the appropriate set-points for the relevant motors and for the fan. Feedback from the pressure sensor and localization will be used to close the loop on this system and simplify the interface for the end user.

5.5.3 Control Flow

In order to design the user interface for the end user, a preliminary control approach has been outlined in Figure 33. This approach uses PID (proportional, integral, and derivative) control for both the fan and the motor PWM signals. The pressure sensor and the localization velocity sensor close the loop for control of the fan and motor respectively, allowing the system to meet the desired reference pressure (modeled in Section 3) and velocities. The fan and motors are controlled by separate controllers and feedback loops, but connect in the "Tip Eversion" block to show that both have an impact on the tip velocity of the robot.

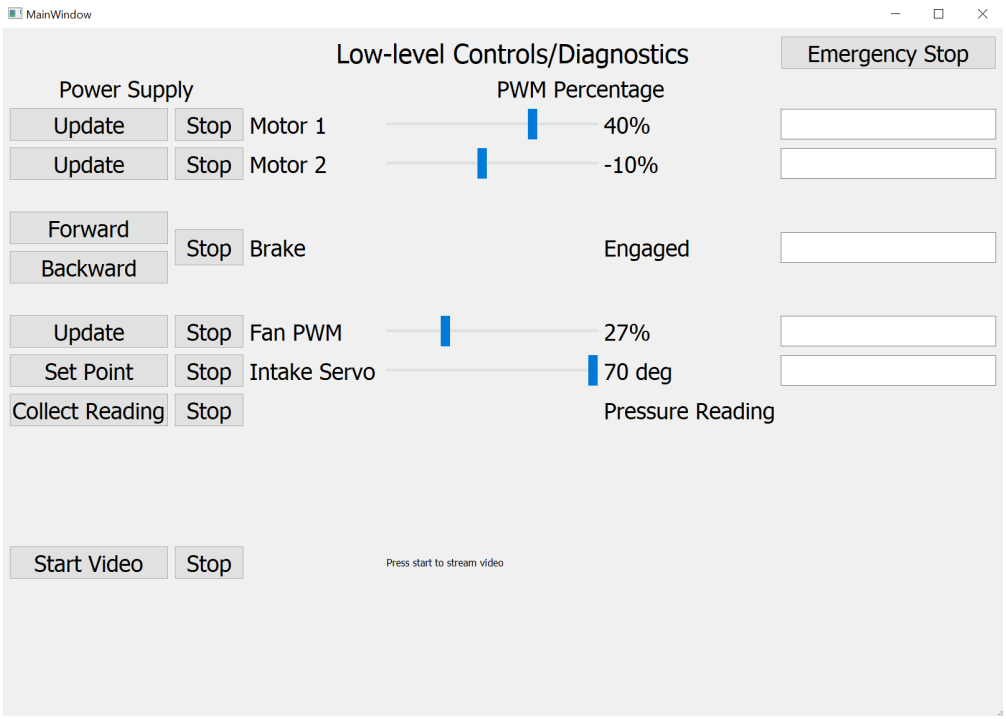

Figure 32: Screenshot of UI for diagnostics testing.

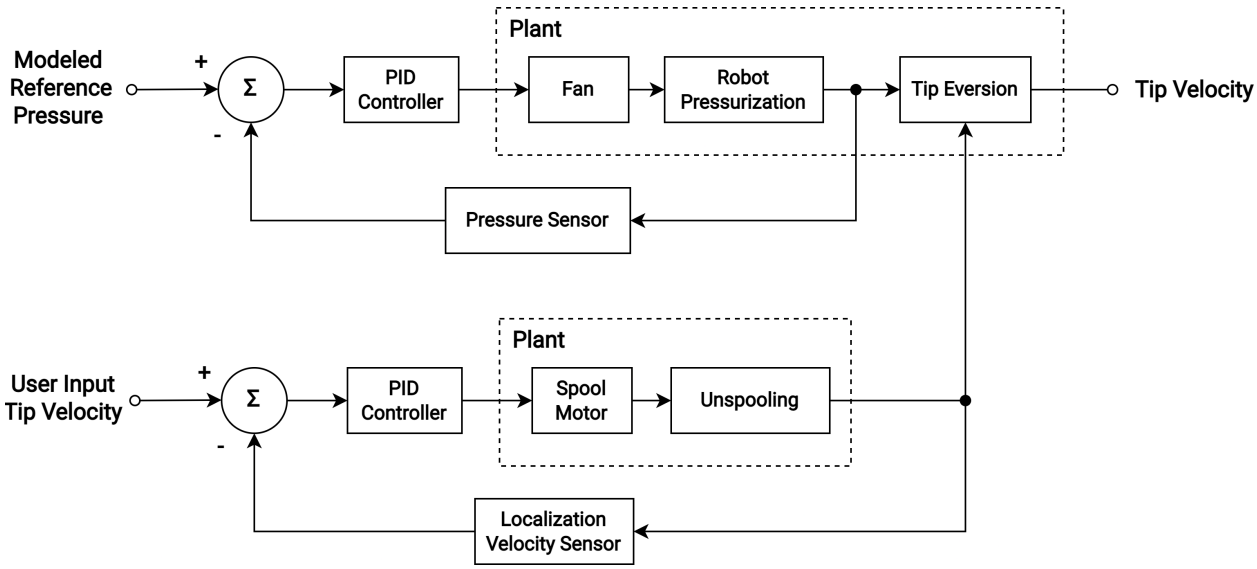

Figure 33: Control scheme for controlling fan and spool motors using feedback from sensors.

5.6 Final Product

TBD - Final product has not yet been created

5.6.1 Bill of Materials

ITEM NO.	PART NUMBER	DESCRIPTION	QTY.
1	9001K764	Architectural 6063 Aluminum U-Channel	1
2	Custom_Motor	Fabric Brushed DC Motor	1
3	6508T52	Two-Piece Shaft Coupling	1
4	3445N121	Easy-to-Machine 1144 Carbon Steel Rod	1
5	4592T318	Anodized Architectural 6063 Aluminum U Channel Aluminum U-Channel	1
6	6063K14	Clamping Two-Piece Shaft Collar	2
7	6389K726	Light Duty Dry-Running Nylon Sleeve	
8	Spool	Fabric Spool	1
9	37d-gearmotor-6-10	Ethernet Brushed DC Motor	1
10	1482K62	Rotary Shaft	1
11	6389K706	Light Duty Dry-Running Nylon Sleeve	
12	6063K13	Clamping Two-Piece Shaft Collar	3
13	Ethernet spool	Ethernet Spool	1
14	88805K219	Architectural 6063 Aluminum 90 Degree Angle	1
15	6508T51	Two-Piece Shaft Coupling	1
16	6389K707	Light Duty Dry-Running Nylon Sleeve Bearing	2
17	Aluminum plate	For Spool Walls	2
18	Plastic plate	3D Printed Spacer	2
19	Center_Piece	3D Printed Spacer	1
20	9604T11	Flange-Mount Shaft Collar	2
21	9604T12	Flange-Mount Shaft Collar	2
22	98689A112	General Purpose 18-8 Stainless Steel Washer	13
23	98269A430	Black-Oxide 18-8 Stainless Steel Washer	19

Table 4: Bill of Materials

ITEM NO.	PART NUMBER	DESCRIPTION	QTY.
24	90348A012	18-8 Stainless Steel Socket Head Screws	19
25	91290A117	Alloy Steel Socket Head Screw	7
26	91290A171	Black-Oxide Alloy Steel Socket Head Screw	15
27	96765A223	Black-Oxide 18-8 Stainless Steel Washer	89
28	94407A114	18-8 Stainless Steel Nylon-Insert Locknut	64
29	4630T208	Anodized Architectural 6063 Aluminum 90 Degree Angle	1
30	1434K84	Mounted Roller Bearing with Two-Bolt Flange	2
31	1434K83	Mounted Roller Bearing with Two-Bolt Flange	2
33	98689A114	General Purpose 18-8 Stainless Steel	1
34	90591A260	Zinc-Plated Steel Hex Nut	6
35	Plastic plate 2	3D Printed Spacer	1
36	Plastic plate 2.2	3D Printed Spacer	1
37	Router	Ethernet Router	1
38	Aluminum plate 2	For Spool Walls	2
40	91290A231	Alloy Steel Socket Head Screw	6
41	Bolt_Plate	Intake Bolt Plate	3
42	Bolt_Plate_Side	Intake Bolt Plate	6
43	91864A050	Black-Oxide Alloy Steel Socket Head Screw	12
44	90576A102	Medium-Strength Steel Nylon-Insert Locknut	4
45	6436K14	Clamping Two-Piece Shaft Collar	4
46	8547K62	Chemical-Resistant Slippery PTFE Tube	2
47	Baseplate	Baseplate	1
48	7208K51	Low-Profile Mounted Sealed Steel	1
49	89955K441	Easy-to-Weld 4130 Alloy Steel	1
50	4630T206	Anodized Architectural 6063 Aluminum 90 Degree Angle	2
51	7208K51	Low-Profile Mounted Sealed Steel Ball Bearing	2
52	90576A212	Medium-Strength Steel Nylon-Insert Locknut	6
53	3D Printed bracket	Structural Support Bracket	2
54	91290A162	Alloy Steel Socket Head Screw	6

Table 5: Bill of Materials Continued

ITEM NO.	PART NUMBER	DESCRIPTION	QTY.
55		Acrylic Front_Plate	1
56		3D printed Front_Spacer_Block	4
57	94510A412	Brass Screw-to-Expand Inserts	2
58		Front_Bolt_Plate	1
59		Black-Oxide Alloy Steel Socket	18
60		Low-Profile Mounted Shielded Steel	6
61		Front_Bearing_Spacer	6
62	94510A030	Brass Screw-to-Expand Inserts	13
63		Ethernet Spool Axle	3
64		Fan model	1
65		Fan_inlet_adaptor	1
66		Fan_inlet_adaptor 2	1
67		Intake Box	1
68		Exhaust Box	1
69		Exhaust Door	1
70		Intake Door	1
71		3D printed servo gear	1
72		3D printer connector	1
73		Servo Motor	1
74		3D printed servo housing	1
75		3D printed servo mount	1
76		3D printer Gear	2
77		Fan Mechanism Bushing	4
78		Intake Adaptor	1
79		Fan Box	1
80		Vertical Fan Mech. Box Support	2
81		Fan bracket	1
82		Horizontal Fan Mech. Box Support	1
83		Fan Mech. Box Support Beam	1
84	8632T139	D-Profile Rotary Shaft	1
85	8632T139	D-Profile Rotary Shaft	1
86		Vine Robot Body	1
87		48V Power Supply	1
88		24V High Current H-Bridge	3
89		High Voltage Buck Converter	3
90		Low Voltage Buck Converter	2
91		Electronic Box	1
92		Busbar	1
93		Power Switch	1

Table 6: Bill of Materials Continued

ITEM NO.	PART NUMBER	DESCRIPTION	QTY.
94		Raspberry Pi Pico W	1
95		USB 5V Buck Converter	1
96		Backplate Interface	1
97		Backplate Bracket Interface	2
98		Backinterface_Bolt	1
99		Vinyl Bag	1
100	4592T243	Anodized Architectural 6063 Aluminum U- Channel	1
101	4592T243	Anodized Architectural 6063 Aluminum U- Channel	1
102	4592T243	Anodized Architectural 6063 U-Channel	1
103	4592T243	Anodized Architectural 6063 Aluminum U-Channel	1
104		Bag Bracket	2
105	1590A55_Draw Latch	Draw Latch	2
106		Large Vent	1
107		Medium vent	1
108		Small vent	1
109		Vertical Placement_Block	1
110		Horizontal Placement_Block	1
111		Placement_Block_2	1
112	9546K205	Heavy Duty Threaded-Stud Bumper	10
113	90640A129	Low-Strength Steel Nylon-Insert Locknut	2
114	96765A140	Black-Oxide 18-8 Stainless Steel Washer	1
115	97135A414	High-Strength Steel Nylon-Insert Locknut	1
116	6435K11	Clamping Shaft Collar	6
117		Base Station Mounting Block	
118		Molex Pin Mount	3
119		Back Connector	3
120		9-Pin Connector Mount	1
121		Baseplate	1
122		Bearing_Sleeve	5
123	57155K382	Stainless Steel Ball Bearing	10
124		Aluminum Axle	10

Table 7: Bill of Materials Continued

5.6.2 Budget

Source:	Value($)
CNSI grant	$3,000
URCA grant	$740
Bechtel grant	$10,000
Edison grant	$2,000
Lucas grant	$1,000
Total	$16,740

Table 8: Funding

Item	Cost ($)
Base station v.1	$841.13
Base station v.2	$2,338.48
Tip mount v.1	$192.26
Tip mount v.2	$330.72
Communications	$649.53
Vine Robot Body	$494.66
Vine robot Body V.2	TBD
General Supplies	$2,605.05
Total	$7,451.83

Table 9: Costs

5.6.3 Gantt Chart

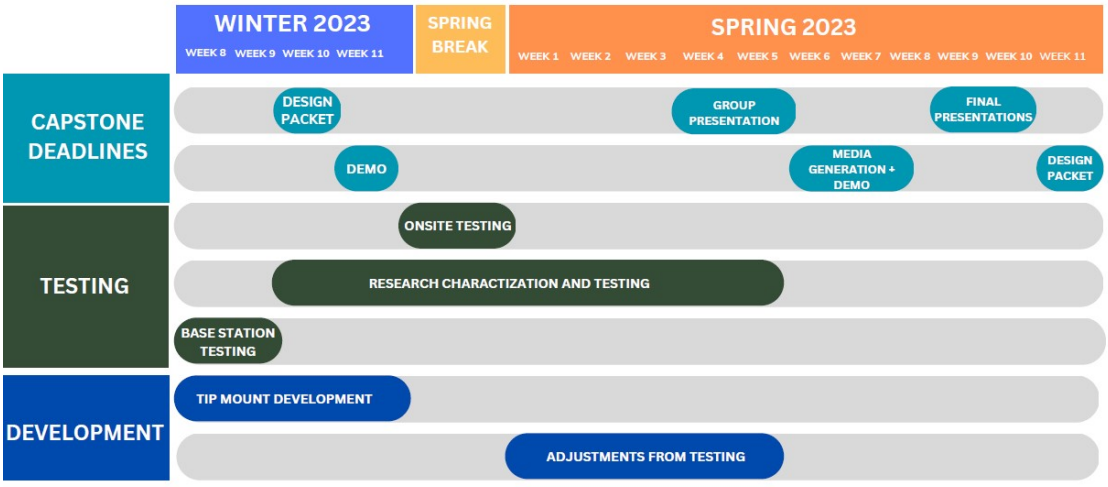

Figure 34: Gantt chart of Winter and Spring quarters.

Future and past work for this project is outlined in the gantt chart above. The last few weeks were spent testing the base station, developing the tip mount, and documenting findings in both the design review and the design packet. Looking ahead, the plan is to continue testing the base

station and auxiliary assemblies, then adjust the design accordingly. A key step in our plan is to conduct onsite testing at the Bechtel Headquarters which is outlined in greater detail in Section 6.

6 Testing and Validation

6.1 Test Site

The testing site for this project corresponds to "Task 1" outlined by Bechtel Corporation. Task one consists of the inspection of a 160 ft. pipe with a 90-degree turn and a 40 ft. vertical section.

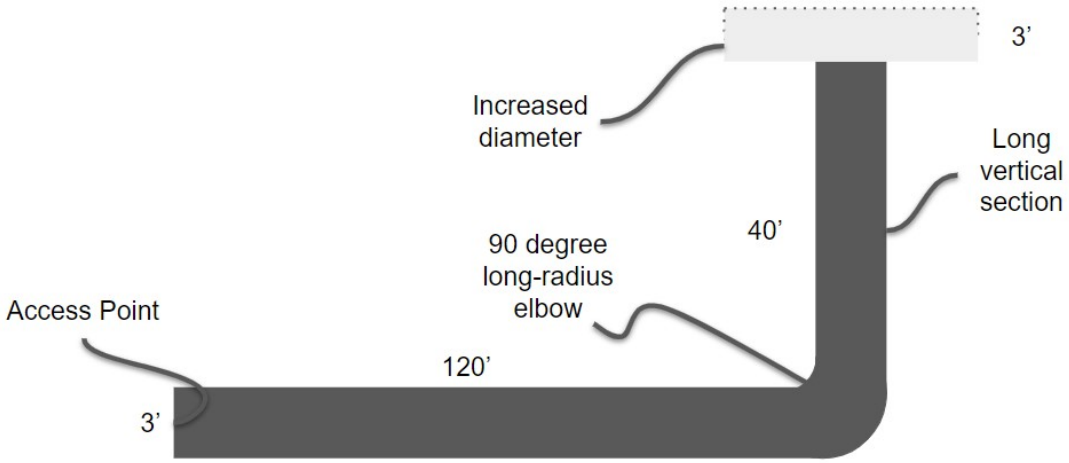

Figure 35: Bechtel Task 1.

The tentative plan is an onsite visit to Bechtel's research facility in Houston. Bechtel has communicated that they will build us a pipe section outlined in "Task 1". Apical Robotics plans to utilize this opportunity to work out design flaws and gain insights that wouldn't be possible without test equipment present.

7 Appendix A - Systems-Level Drawings

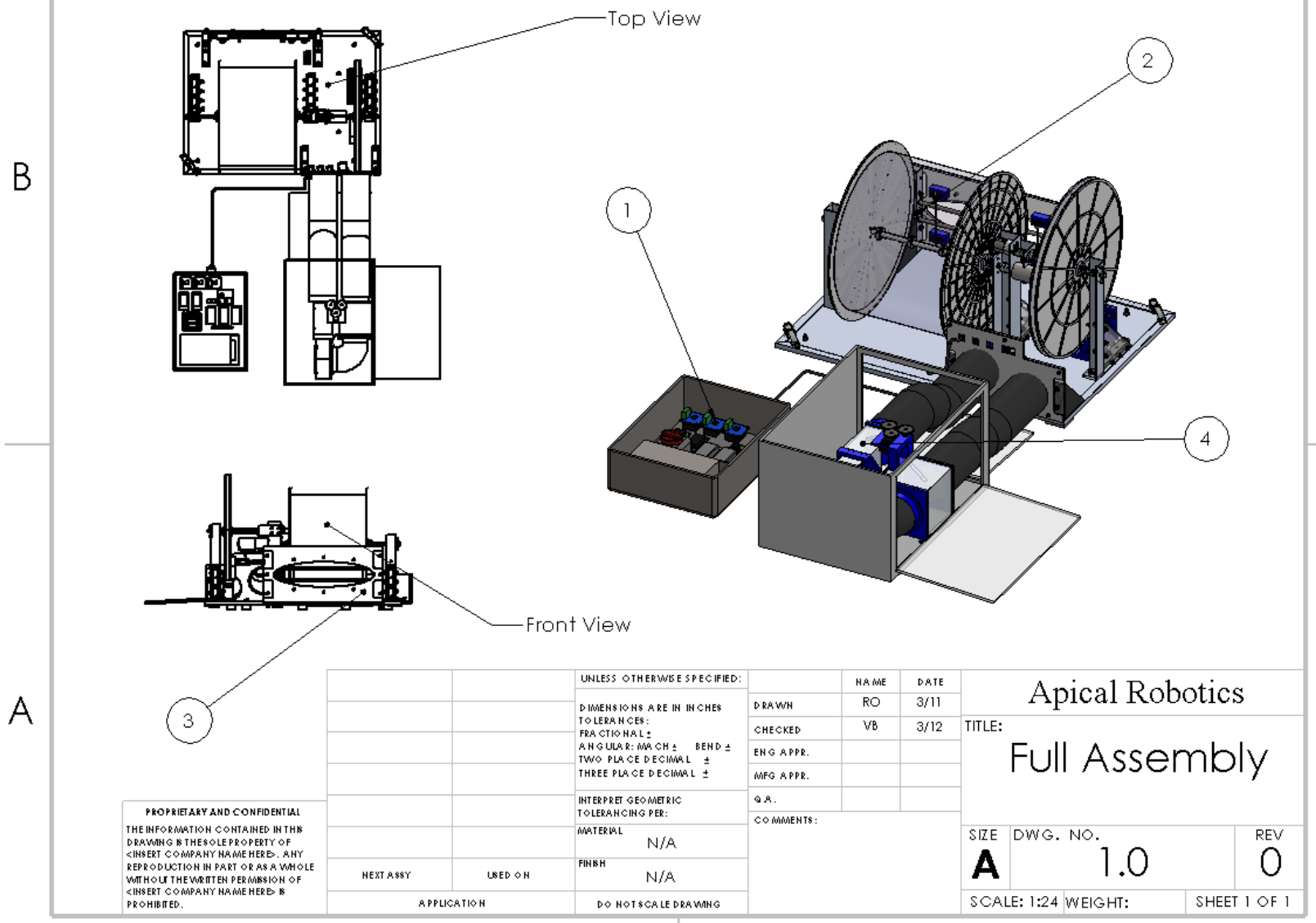

		UNLESS OTHERWISE SPECIFIED:		NAME	DATE	Apical Robotics
		DIMENSIONS ARE IN INCHES TOLERANCES: FRACTIONAL ± ANGULAR: MACH ± BEND ± TWO PLACE DECIMAL ± THREE PLACE DECIMAL ±	DRAWN	RO	3/11	TITLE: Full Assembly
			CHECKED	VB	3/12	
			ENG APPR.			
			MFG APPR.			
		INTERPRET GEOMETRIC TOLERANCING PER:	Q.A.			
		MATERIAL N/A	COMMENTS:			SIZE A / DWG. NO. 1.0 / REV 0
NEXT ASSY	USED ON	FINISH N/A				SCALE: 1:24 WEIGHT: SHEET 1 OF 1
APPLICATION		DO NOT SCALE DRAWING				

Asm Number	Name
1	Electronics
2	Motor Spool
3	Fabric Intake
4	Fan Mechanism

8 Appendix B - Sub-System Level Drawings

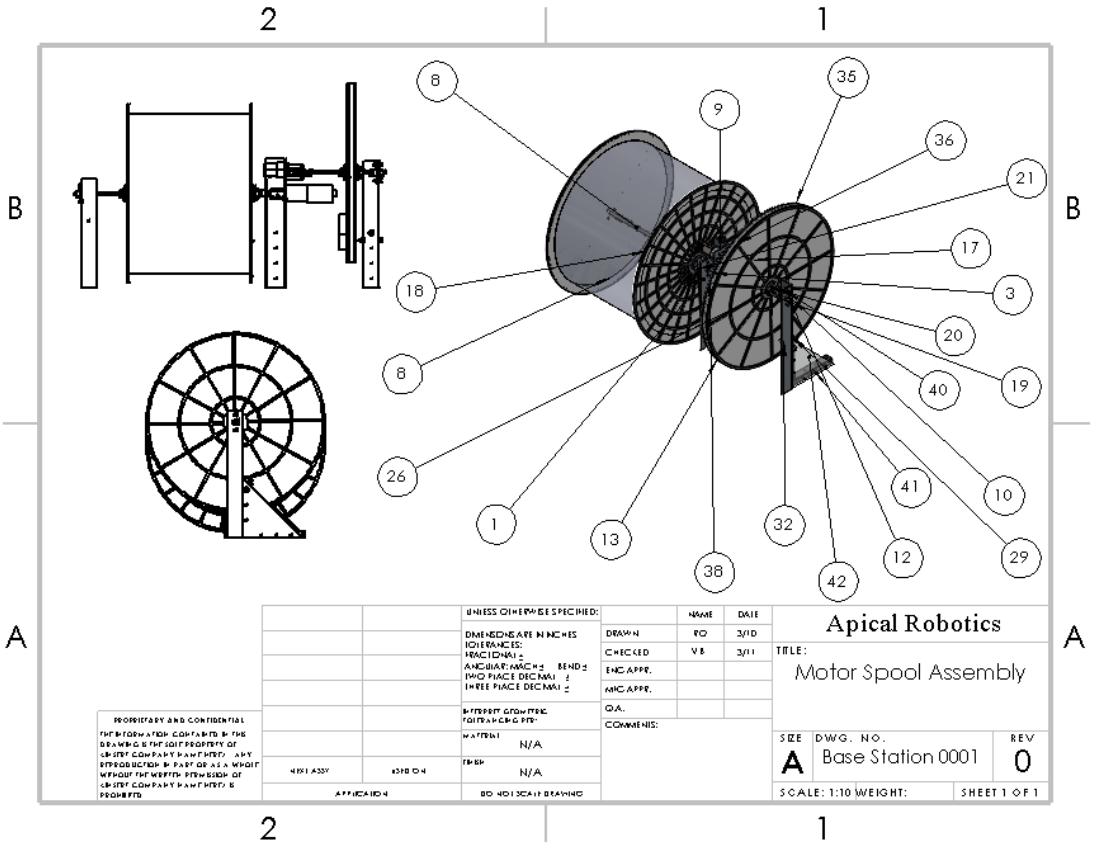

ITEM NO.	PART NUMBER	DESCRIPTION	QTY.
1	9001K764	Architectural 6063 Aluminum U-Channel	1
3	6508T52	Two-Piece Shaft Coupling	1
8	Spool		1
9	37d-gearmotor-6-10		1
10	1482K62	Rotary Shaft	1
12	6063K13	Clamping Two-Piece Shaft Collar	3
13	ethernet spool		1
17	aluminum plate		2
18	plastic plate		2
19	Center_Piece		1
20	9604T11	Flange-Mount Shaft Collar	2
21	9604T12	Flange-Mount Shaft Collar	2
25	91290A117	Alloy Steel Socket Head Screw	7
26	91290A171	Black-Oxide Alloy Steel Socket Head Screw	3
32	91251A889	Black-Oxide Alloy Steel Socket Head Screw	1
35	plastic plate 2		1
36	plastic plate 2.2		1
38	aluminum plate 2		2
40	91290A231	Alloy Steel Socket Head Screw	6
41	Bolt_Plate		3
42	Bolt_Plate_Side		6

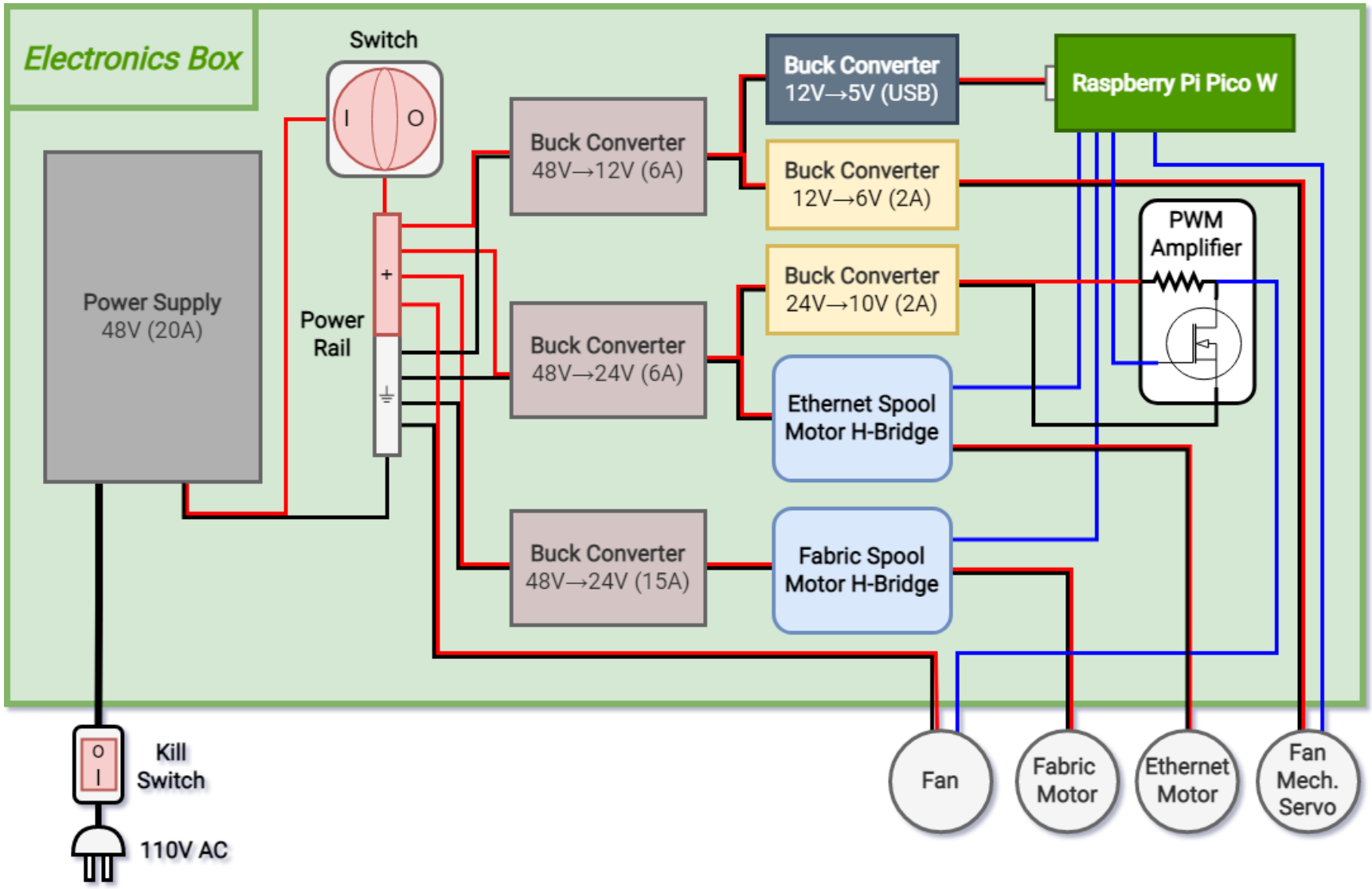
Electronics Box
Switch
I
O
Power Supply
48V (20A)
Power
Rail
+
Buck Converter
48V→12V (6A)
Buck Converter
48V→24V (6A)
Buck Converter
48V→24V (15A)
Buck Converter
12V→5V (USB)
Buck Converter
12V→6V (2A)
Buck Converter
24V→10V (2A)
Ethernet Spool
Motor H-Bridge
Fabric Spool
Motor H-Bridge
Raspberry Pi Pico W
PWM
Amplifier
O
I
Kill
Switch
110V AC
Fan
Fabric
Motor
Ethernet
Motor
Fan
Mech.
Servo

ITEM NO.	PART NUMBER	DESCRIPTION	QTY.
1	7208K51	Low-Profile Mounted Sealed Steel Ball Bearing	4
2	89955K441	Easy-to-Weld 4130 Alloy Steel Round Tube	2
3	4630T206	Anodized Architectural 6063 Aluminum 90 Degree Angle	2
6	3dprintbracket		2
7	91290A162	Alloy Steel Socket Head Screw	1
8	Front_Plate		1
9	Front_Spacer_Block		4
11	Front_Bolt_Plate		1
12	91251A454	Black-Oxide Alloy Steel Socket Head Screw	1
14	90348A012	18-8 Stainless Steel Socket Head Screws	1
15	98269A430	Black-Oxide 18-8 Stainless Steel Washer	1
17	94407A114	18-8 Stainless Steel Nylon-Insert Locknut	2
19	8600N1	Low-Profile Mounted Shielded Steel Ball Bearing	6

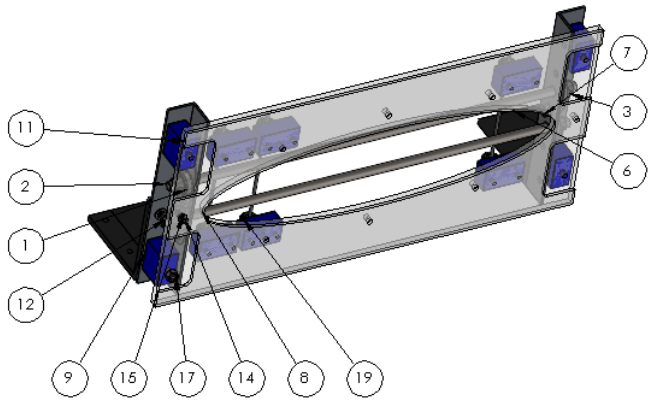

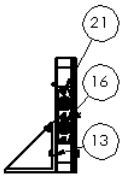

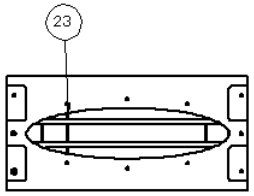

		UNLESS OTHERWISE SPECIFIED:		NAME	DATE
		DIMENSIONS ARE IN INCHES TOLERANCES: FRACTIONAL ± ANGULAR: MACH ± BEND ± TWO PLACE DECIMAL ± THREE PLACE DECIMAL ±	DRAWN	RO	3/10
			CHECKED	VB	3/11
			ENG APPR.		
			MFG APPR.		
		NEXT PART GEOMETRIC TOLERANCING PER:	Q.A.		
		MATERIAL N/A	COMMENTS:		
NEXT ASSY	USED ON	FINISH N/A			
APPLICATION		DO NOT SCALE DRAWING			

Apical Robotics

TITLE:

Fabric Intake

SIZE	DWG. NO.	REV
B	Base Station 0002	0

SCALE: 1:8 | WEIGHT: | SHEET 1 OF 1

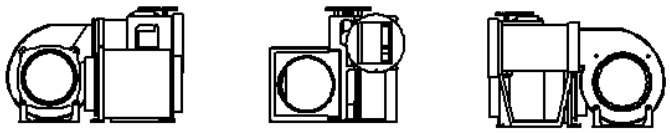

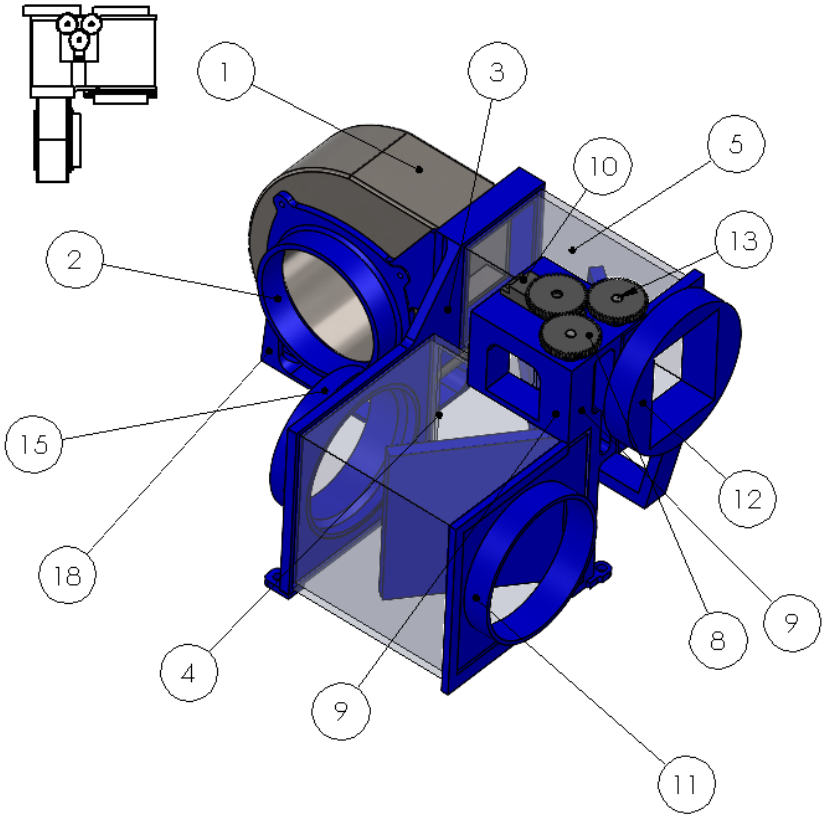

ITEM NO.	PART NUMBER	DESCRIPTION	QTY.
1	new fan model		1
2	fan_inlet_adaptor		1
3	fan_inlet_adaptor 2		1
4	intakeBox		1
5	exhaustBox		1
8	6832K56	Metal Gear - 20 Degree Pressure Angle	2
9	Gear Mount Platform		1
10	Servo		1
11	Intake Adapter		1
12	Exhaust Adapter		1
13	6832K56	Metal Gear - 20 Degree Pressure Angle	1
15	intake adapt adaptor		1
18	fan bracket		1

NEXT ASSY	USED ON	
APPLICATION		DO NOT SCALE DRAWING

UNLESS OTHERWISE SPECIFIED:

DIMENSIONS ARE IN INCHES
TOLERANCES:
FRACTIONAL ±
ANGULAR: MACH ± BEND ±
TWO PLACE DECIMAL ±
THREE PLACE DECIMAL ±

INTERPRET GEOMETRIC TOLERANCING PER:

MATERIAL N/A

FINISH N/A

	NAME	DATE
DRAWN	RO	3/10
CHECKED	VB	3/11
ENG APPR.		
MFG APPR.		
Q.A.		

COMMENTS:

Apical Robotics

TITLE:

Fan Mechanism

SIZE	DWG. NO.	REV
A	Base Station 0003	0

SCALE: 1:8 | WEIGHT: | SHEET 1 OF 1

ITEM NO.	PART NUMBER	DESCRIPTION	QTY.
1	backinterface		1
2	91251A454	Black-Oxide Alloy Steel Socket Head Screw	1
3	94407A114	18-8 Stainless Steel Nylon-Insert Locknut	1
4	3dprintbracket_Backinterface		2
5	backinterface_Bolt		1
6	94510A412	Brass Screw-to-Expand Inserts	1
7	90348A012	18-8 Stainless Steel Socket Head Screws	1
8	98269A430	Black-Oxide 18-8 Stainless Steel Washer	1
9	96765A223	Black-Oxide 18-8 Stainless Steel Washer	2

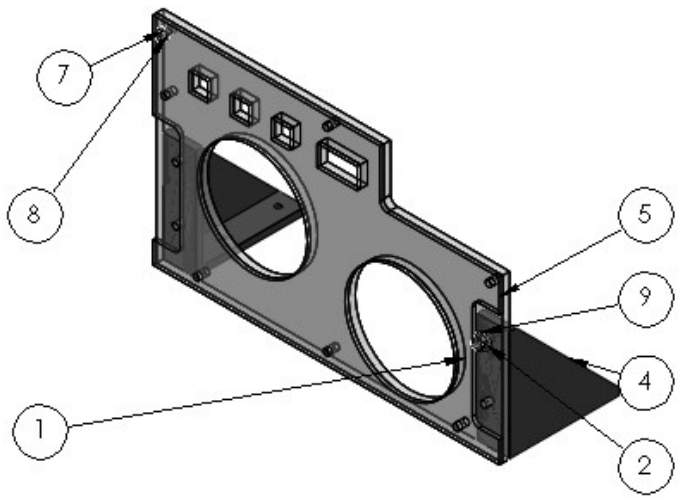

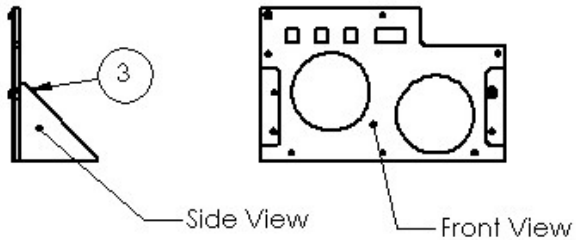

NEXT ASSY	USED ON	
APPLICATION		

UNLESS OTHERWISE SPECIFIED:
DIMENSIONS ARE IN INCHES
TOLERANCES:
FRACTIONAL ±
ANGULAR: MACH ± BEND ±
TWO PLACE DECIMAL ±
THREE PLACE DECIMAL ±
INTERPRET GEOMETRIC TOLERANCING PER:
MATERIAL N/A
FINISH N/A
DO NOT SCALE DRAWING

	NAME	DATE
DRAWN	RO	3/13
CHECKED	VB	3/13
ENG APPR.		
MFG APPR.		
Q.A.		
COMMENTS:		

Apical Robotics

TITLE: Backplate Assembly

SIZE	DWG. NO.	REV
A	Base Station 0004	0

SCALE: 1:4 | WEIGHT: | SHEET 1 OF 1

9 Appendix C - Detailed Drawings

Drawings of 3D printed and laser-cut parts are omitted since these manufacturing processes do not require an engineering drawing and are carried out directly based on the 3D models.

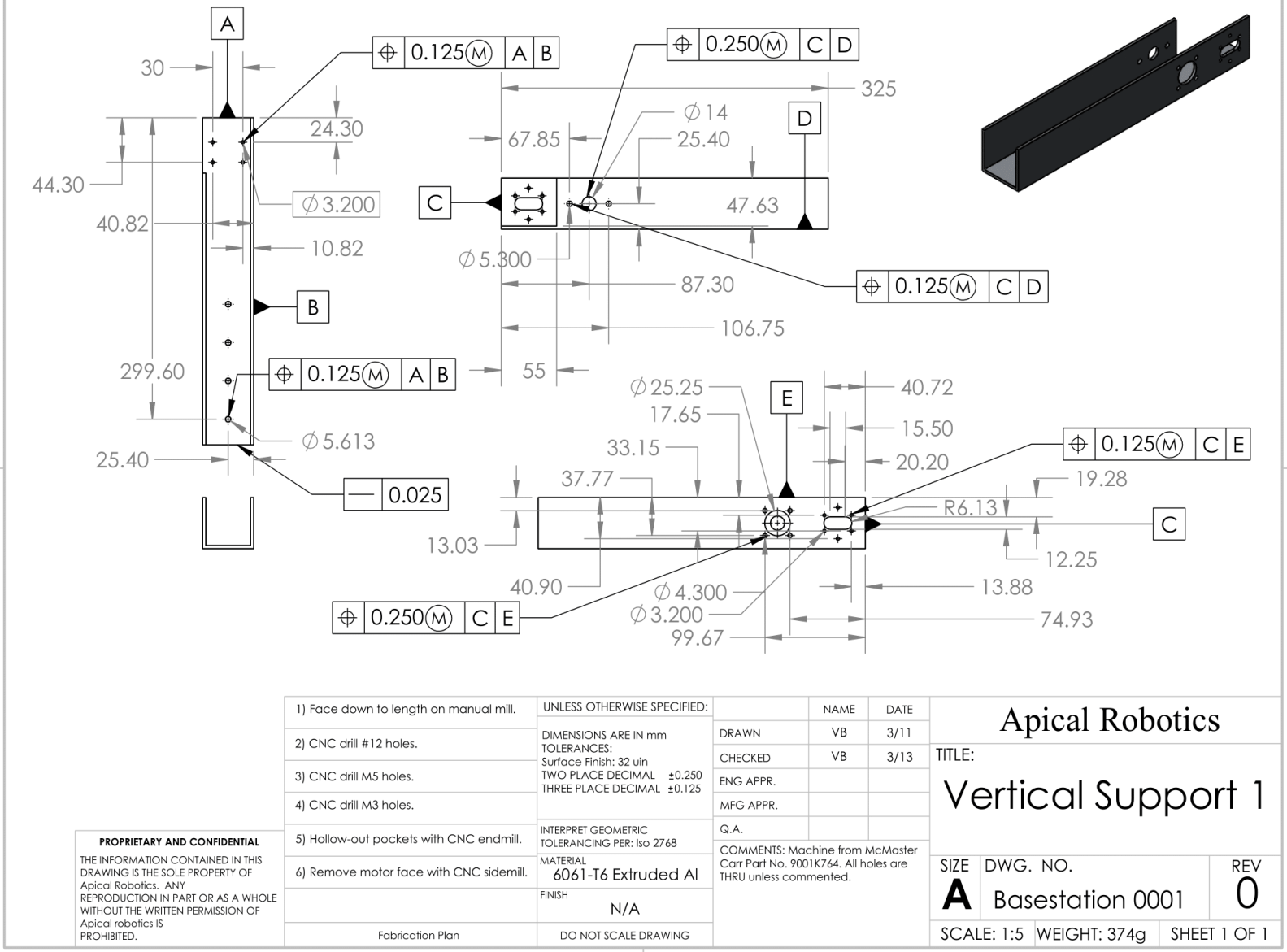

1) Face down to length on manual mill.	UNLESS OTHERWISE SPECIFIED:		NAME	DATE	Apical Robotics
2) CNC drill #12 holes.	DIMENSIONS ARE IN mm TOLERANCES: Surface Finish: 32 uin TWO PLACE DECIMAL ±0.250 THREE PLACE DECIMAL ±0.125	DRAWN	VB	3/11	TITLE: Vertical Support 1
3) CNC drill M5 holes.		CHECKED	VB	3/13	
4) CNC drill M3 holes.		ENG APPR.			
5) Hollow-out pockets with CNC endmill.	INTERPRET GEOMETRIC TOLERANCING PER: Iso 2768	MFG APPR.			
6) Remove motor face with CNC sidemill.	MATERIAL 6061-T6 Extruded Al	Q.A.			SIZE A | DWG. NO. Basestation 0001 | REV 0
	FINISH N/A	COMMENTS: Machine from McMaster Carr Part No. 9001K764. All holes are THRU unless commented.			SCALE: 1:5 | WEIGHT: 374g | SHEET 1 OF 1
Fabrication Plan	DO NOT SCALE DRAWING				

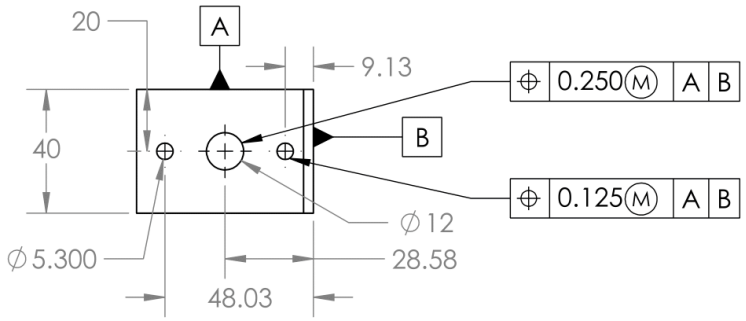

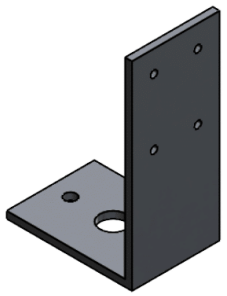

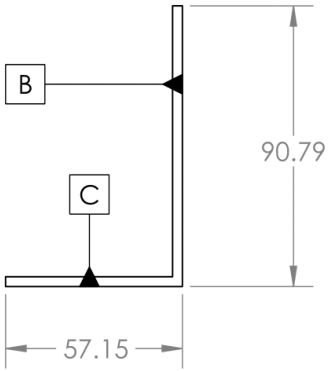

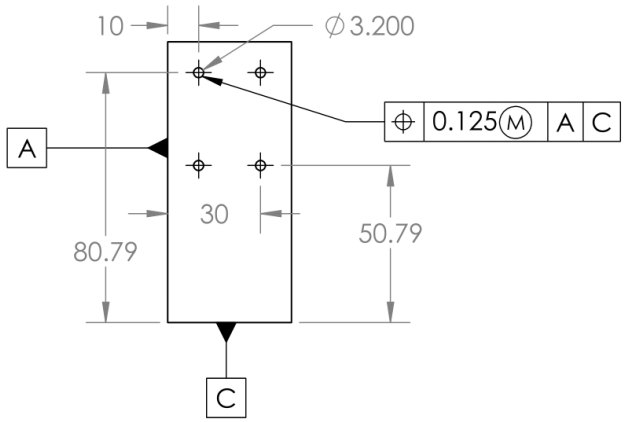

1) Cut to rough length with bandsaw.	UNLESS OTHERWISE SPECIFIED:		NAME	DATE
2) Face down to length with CNC mill.	DIMENSIONS ARE IN mm TOLERANCES: Surface Finish: 32un TWO PLACE DECIMAL ±0.250 THREE PLACE DECIMAL ±0.125	DRAWN	WH	3/11
3) CNC drill M5 holes.		CHECKED	VB	3/13
4) CNC drill M3 holes.		ENG APPR.		
		MFG APPR.		
5) Clear out pocket with CNC endmill.	INTERPRET GEOMETRIC TOLERANCING PER: Iso 2768	Q.A.		
	MATERIAL 6061-T6 Extruded Al	COMMENTS: Machined from McMaster Carr Part No. 88805k219. All holes are THRU unless commented.		
	FINISH N/A			
Fabrication Plan	DO NOT SCALE DRAWING			

Apical Robotics

TITLE:

Motor Mount

SIZE	DWG. NO.	REV
A	Basestation 0002	0

SCALE: 1:2 | WEIGHT: 48g | SHEET 1 OF 1

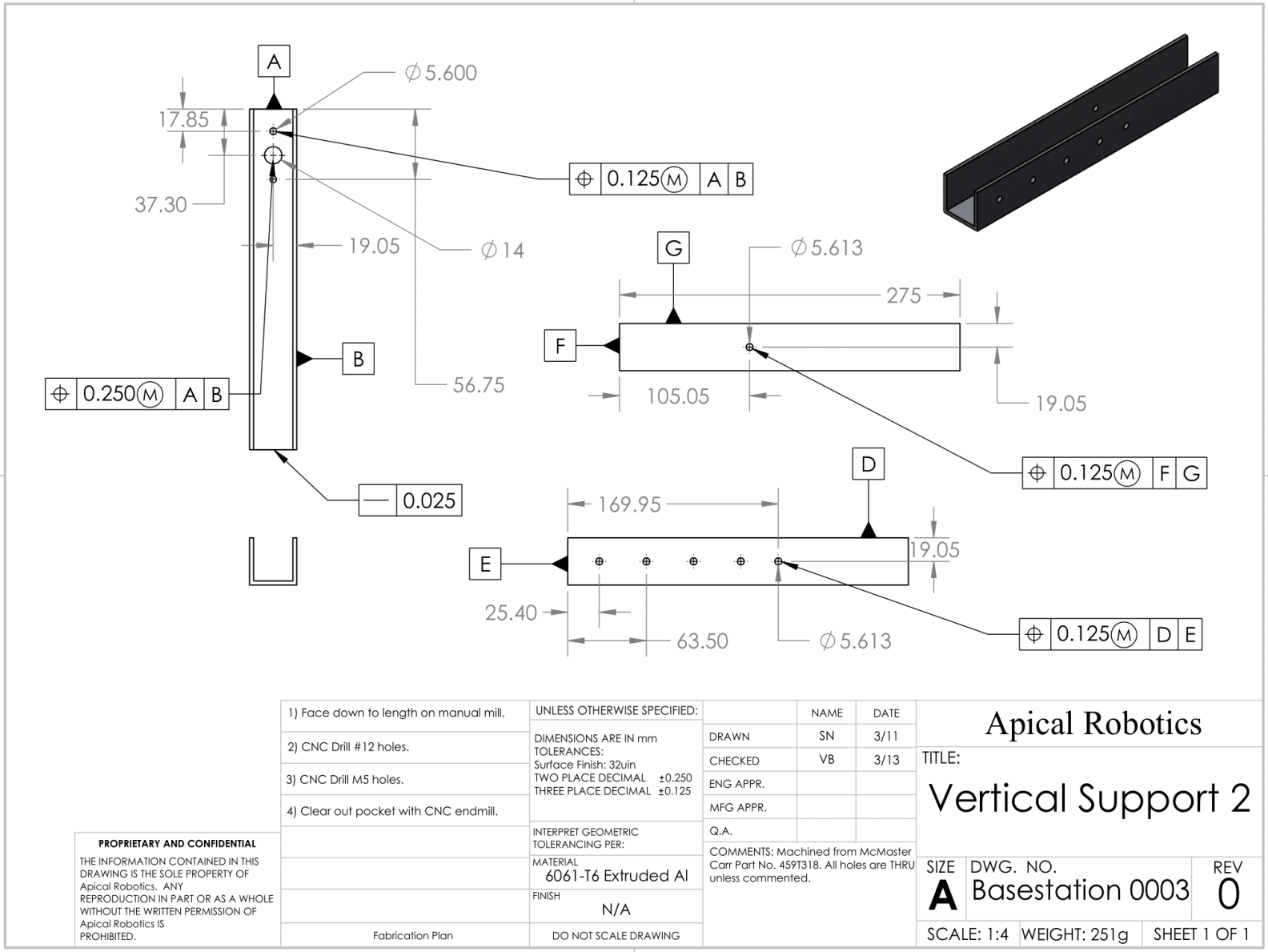

1) Face down to length on manual mill.	UNLESS OTHERWISE SPECIFIED:		NAME	DATE	Apical Robotics
2) CNC Drill #12 holes.	DIMENSIONS ARE IN mm TOLERANCES: Surface Finish: 32uin TWO PLACE DECIMAL ±0.250 THREE PLACE DECIMAL ±0.125	DRAWN	SN	3/11	TITLE:
3) CNC Drill M5 holes.		CHECKED	VB	3/13	Vertical Support 2
4) Clear out pocket with CNC endmill.		ENG APPR.			
		MFG APPR.			
	INTERPRET GEOMETRIC TOLERANCING PER:	Q.A.			
	MATERIAL 6061-T6 Extruded Al	COMMENTS: Machined from McMaster Carr Part No. 459T318. All holes are THRU unless commented.			SIZE A / DWG. NO. Basestation 0003 / REV 0
	FINISH N/A				SCALE: 1:4 / WEIGHT: 251g / SHEET 1 OF 1
Fabrication Plan	DO NOT SCALE DRAWING				

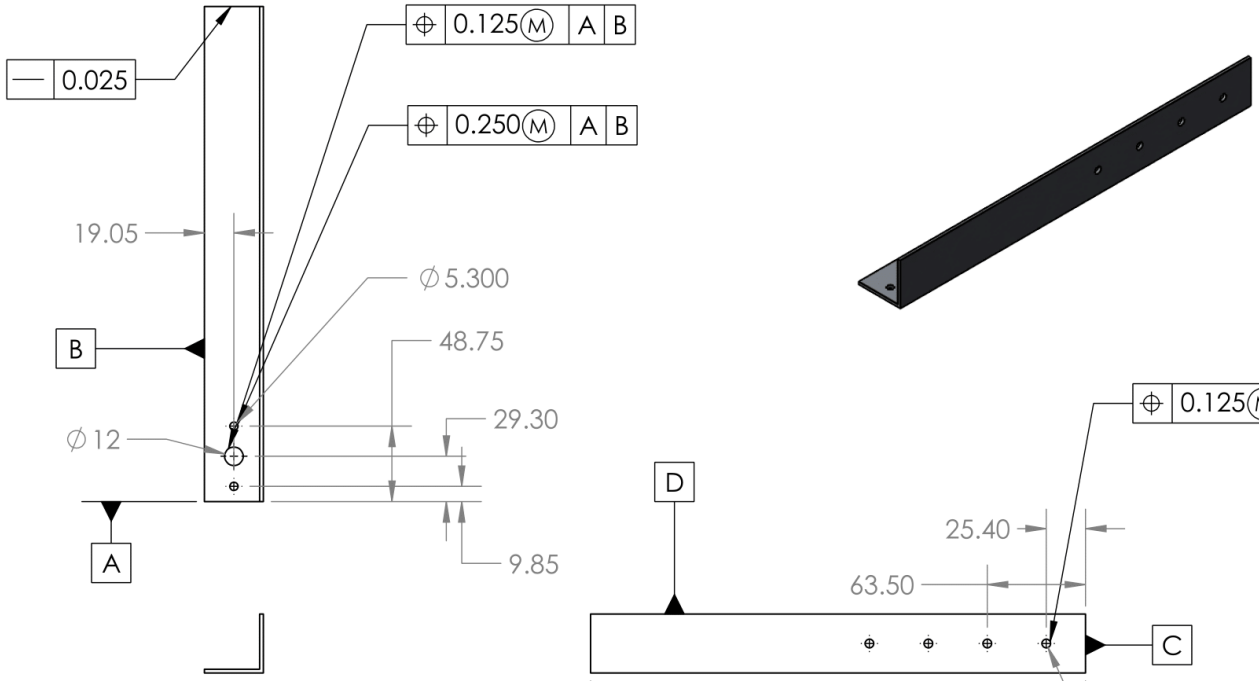

1) Face down to length on CNC mill.

2) CNC drill #12 holes.

3) Clear out pocket with CNC endmill.

UNLESS OTHERWISE SPECIFIED:

DIMENSIONS ARE IN mm
TOLERANCES:
Surface Finish: 32uin
TWO PLACE DECIMAL ±0.250
THREE PLACE DECIMAL ±0.125

INTERPRET GEOMETRIC TOLERANCING PER: Iso 2768

MATERIAL
6061-T6 Extruded Al

FINISH
N/A

DO NOT SCALE DRAWING

Fabrication Plan

	NAME	DATE
DRAWN	RO	3/11
CHECKED	VB	3/13
ENG APPR.		
MFG APPR.		
Q.A.		

COMMENTS: Machined from McMaster Carr Part No. 4630T208. All holes are THRU unless commented.

Apical Robotics

TITLE:

Vertical Support 3

SIZE	DWG. NO.	REV
A	Basestation 0004	0

SCALE: 1:4 | WEIGHT: 150g | SHEET 1 OF 1

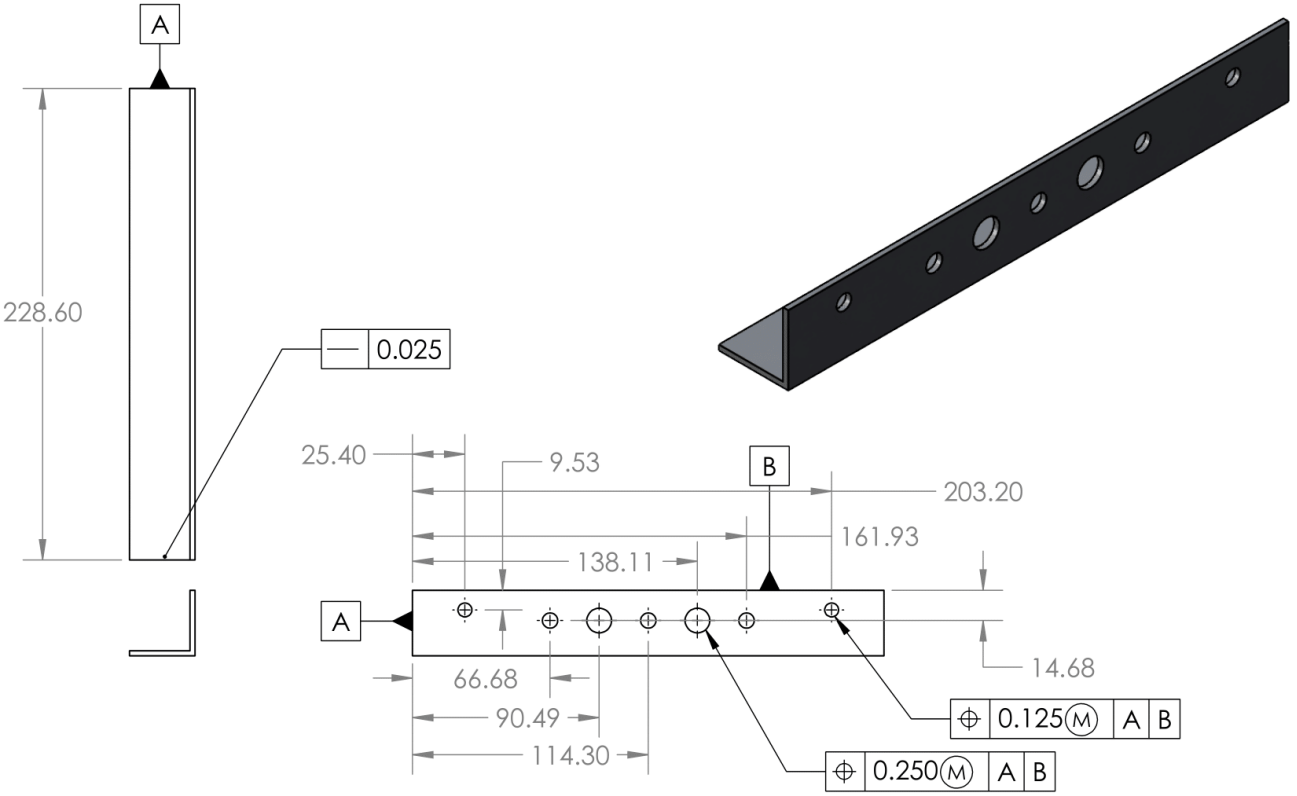

1) Face down to length with manual mill.	UNLESS OTHERWISE SPECIFIED:		NAME	DATE	Apical Robotics
2) CNC drill #12 clearance holes.	DIMENSIONS ARE IN mm TOLERANCES: Surface Finish: 32uin TWO PLACE DECIMAL ±0.250 THREE PLACE DECIMAL ±0.125	DRAWN	SM	3/11	TITLE: Vertical Support 4
3) Create pockets with CNC endmill.		CHECKED	VB	3/13	
		ENG APPR.			
		MFG APPR.			
	INTERPRET GEOMETRIC TOLERANCING PER: Iso 2768	Q.A.			
	MATERIAL 6061-T6 Extruded Al	COMMENTS: Machined from McMaster Carr Part No. 463T206. All holes are THRU unless commented.			SIZE A | DWG. NO. Basestation 0005 | REV 0
	FINISH N/A				SCALE: 1:4 | WEIGHT: 45g | SHEET 1 OF 1
Fabrication Plan	DO NOT SCALE DRAWING				

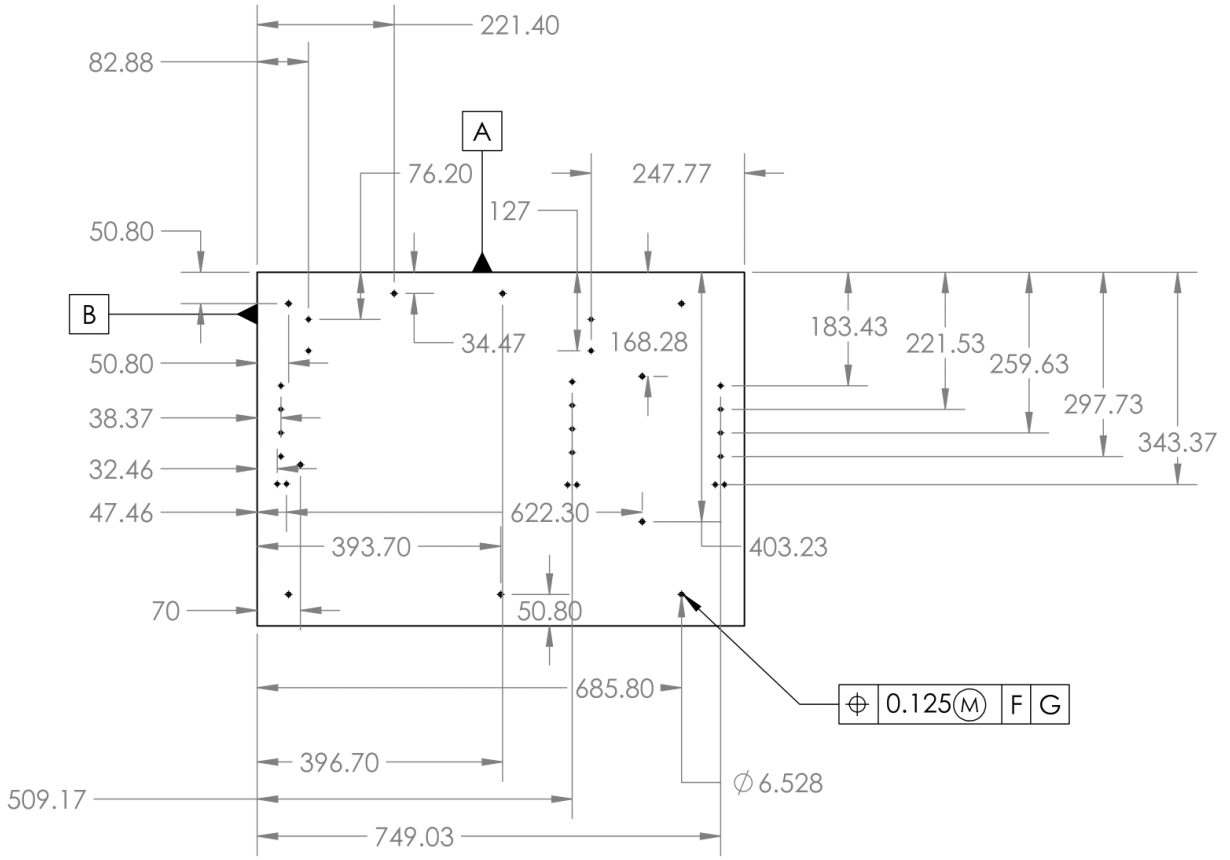

1) Clear-out holes with water-jet cutter.	UNLESS OTHERWISE SPECIFIED:		NAME	DATE
	DIMENSIONS ARE IN mm TOLERANCES: Surface Finish: 32un TWO PLACE DECIMAL ±0.250 THREE PLACE DECIMAL ±0.125	DRAWN	VB	3/11
		CHECKED	VB	3/13
		ENG APPR.		
		MFG APPR.		
	INTERPRET GEOMETRIC TOLERANCING PER: Iso 2768	Q.A.		
	MATERIAL 1/8" 6063 Al	COMMENTS: Machined from 1/8" Al plate. All holes are THRU unless commented.		
	FINISH N/A			
Fabrication Plan	DO NOT SCALE DRAWING			

Apical Robotics

TITLE:

Baseplate

SIZE	DWG. NO.	REV
A	Basestation 0006	0

SCALE: 1:2 | WEIGHT: 8.5lb | SHEET 1 OF 1

10 Appendix D - MATLAB Scripts

Calculate the minimum pressure required to grow through pipe system

```
close all; clc; clear;
run('data_input.m');

%Stage 1: tail and ethernet dragged in the horizontal section [0 - 81.5ft]
S1D = linspace(0,Ls,(Ls*10)+1); %Define the length vector [n ft = 10n + 1
 element]
%Find the tension in the body [N]
S1T = f_factor_silnylon.*S1D + tip_mount_friction + ...
    base_friction_silnylon + f_yield + f_v;
%Find the tension in the ethernet cable [N]
S1Te = f_factor_ethernet.*S1D + base_friction_e;

%Stage 2: tail shortening and replaced by spectra, ethernet dragged in the
%horizontal section [81.5 - 120ft]
S2D = linspace(Ls,Lt,((Lt-Ls)*10)+1); %Define the length vector [n ft = 10n +
 1 element]
%Find the tension in the body [N]
S2T = f_factor_silnylon.*(Ls-(S2D-Ls)) + 2.*f_factor_spectra.*(S2D-Ls)...
+ tip_mount_friction + base_friction_silnylon + f_yield + f_v;
%Find the tension in the ethernet cable [N]
S2Te = f_factor_ethernet.*S2D + base_friction_e;

%Stage 3: entering vertical section with tail shortening and replaced by
%spectra, ethernet draging in the horizontal section [120ft - 141.5ft]
S3D = linspace(Lt,Lv,((Lv-Lt)*10)+1); %Define the length vector [n ft = 10n +
 1 element]
%Find the horizontal tension in the body [N]
S3T = f_factor_silnylon.*((L-Lt)-2.*(S3D-Lt)) + 2.*f_factor_spectra.*(S3D-Ls);
S3Te = f_factor_ethernet.*Lt;
%Account for Capstan friction at the turn
S3T = S3T.*exp((mu_capstan.*pi)./2);
S3Te = S3Te.*exp((mu_capstan.*pi)./2);
%Find the vertical tension in the body [N]
S3T = S3T + w_per_l.*(S3D-Lt) + tip_weight + ...
    base_friction_silnylon + f_yield + f_v;
S3Te = S3Te + w_ethernet_per_l.*(S3D-Lt) + base_friction_e;

%Stage 4: vertical section section after the end of horizontal tail,
% ethernet dragging in the horizontal section [141.5ft - 163 ft]
S4D = linspace(Lv,L,((L-Lv)*10)+1); %Define the length vector [n ft = 10n + 1
 element]
%Find the horizontal tension in the body [N]
S4T = f_factor_spectra.*Lt;
S4Te = f_factor_ethernet.*Lt;
%Account for Capstan friction at the turn
S4T = S4T.*exp((mu_capstan.*pi)./2);
S4Te = S4Te.*exp((mu_capstan.*pi)./2);
%Find the vertical tension in the body [N]
```

```
S4T = S4T + w_per_l.*((L-Lv)-(S4D-Lv)) + tip_weight + ...
    base_friction_silnylon + f_yield + f_v;
S4Te = S4Te + w_ethernet_per_l.*(S4D-Lt) + base_friction_e;

%Combine stages to obtain growth tension requirements
growth_min_T = [S1T S2T S3T S4T];
growth_min_Te = [S1Te S2Te S3Te S4Te];
pipe_length = [S1D S2D S3D S4D];

%Combine stages to obtain growth pressure requirements
P_grow_min = 2*(growth_min_T+growth_min_Te)./A; %[Pa]
P_grow_min_psi = P_grow_min./6894.76; %[psi]

%Safety Factors with respect to burst and yield
pressure_sf = max_pressure_pa./P_grow_min; %[ND]
tensile_sf = max_silnylon_tensile./growth_min_T; %[ND]
lw = 1.5; %Plot line width

% %Plots
% %Figure 1: Tail Tension
% figure;
% plot(pipe_length,growth_min_T,pipe_length,growth_min_Te,'LineWidth',lw);
% ylabel('Tail Tension (N)');
% xlabel('Distance Along Pipe (ft)');
% legend('Body','Cable','location','best');
% title('Tail Tension in Growth');
% set(gca,"FontSize",20)
% print('-dpng','-r300','fig1')
%
% %Figure 2: Min Pressure to Grow
% figure;
% plot(pipe_length,P_grow_min_psi,'LineWidth',lw);
% ylabel('Pressure to grow (psi)');
% xlabel('Distance Along Pipe (ft)');
% title('Required Growth Pressure');
% set(gca,"FontSize",20)
%
% %Figure 3: Tensile Strength Safety Factors
% figure;
% plot(pipe_length,tensile_sf,'LineWidth',lw);
% xlim([50 150]);
% ylabel('Tail Tensile Stress Safety Factor');
% xlabel('Distance Along Pipe (ft)');
% title('Safety Factor for Tensile Tail Failure');
% set(gca,"FontSize",20)
%
% %Figure 4: Burst Pressure Safety Factors
% figure;
% plot(pipe_length,pressure_sf,'LineWidth',lw);
% xlim([50 150]);
% ylabel('Burst Pressure Safety Factor');
% xlabel('Distance Along Pipe (ft)');
% title('Safety Factor for Burst Pressure');
% set(gca,"FontSize",20)
```

Calculate the minimum pressure to grow without buckling

```
close all; clc; clear;
run('data_input.m');
run('growth_pressure.m');

%Constrained growth
P1 = zeros(1,(hv/2)./0.1); %Allocate storage for first half of the pipe
P2 = P1;
i = 1; %Counter

%Stage 3: entering vertical section with tail shortening and replaced by
%spectra, ethernet draging in the horizontal section [120ft - 141.5ft]
for h = Lt:0.1:Lt+(hv/2) %Loop through growth heights
S3Dv = linspace(Lt,h,((h-Lt)*10)+1); %Define the length vector [n ft = 10n + 1
 element]
P1(i) = max((tip_weight + flip(S3Dv-Lt).*(w_per_l) + (h-Lt).*(w_per_l)...
    )./(0.5.*A + (mu_wall.*pi.*D.*(flip(S3Dv-Lt).*0.3048))));
i = i+1;
end

%Stage 4: vertical section section after the end of horizontal tail,
% ethernet dragging in the horizontal section [141.5ft - 163 ft]
i = 1;
for h = Lt+(hv/2):0.1:L
S4Dv = linspace(Lt,h,((h-Lt)*10)+1); %Define the length vector [n ft = 10n + 1
 element]
P2(i) = max((tip_weight + (L-h).*(w_per_l) + ...
    flip(S4Dv-Lt).*(w_per_l))./(0.5.*A + (mu_wall.*pi.*D.*(flip(S4Dv-
Lt).*0.3048))));
i = i+1;
end

%Unconstrained growth
P3 = zeros(1,30); %Allocate storage
hu = linspace(0,3,30); %Linear space for body size
l = hu.*0.3048; %Body length [m]
alpha = atan(0.5*D./(l+hv_m)); %Find angle of tail
r = D./2; %Body radius
body_w = hu.*w_per_l; %Body mass [kg]
T_t = growth_min_T(160*10+1:160*10+30);
%Moment balance equations:
P3_1 = ( tip_weight.*(D.*0.5) + body_w.*(D.*0.5) + ...
    T_t.*(l.*sin(alpha)+D.*0.5.*cos(alpha)) )./(A.*r);
F_axial = T_t.*cos(alpha)+tip_weight+body_w; %Axial Force [N]
P3_2 = P3_1.*A; %Crushing force is equal to pressure force [N]

%Pick the larger value between crushing and transvers buckling
for i = 1:30
    if P3_2(i)>F_axial(i)
```

```
        P3(i) = P3_1(i); %[Pa]
    else
        P3(i) = P3_2(i)./A; %[Pa]
    end
end

%Combine results
P = [P1 P2 P3];
P_psi = P./6894.76;
SDv = linspace(Lt,L,length(P));

% %Plots
% %Figure 5: vertical growth
% figure;
% plot(SDv,P_psi,'LineWidth',lw);
% ylabel('Minimum Required Pressure (psi)');
% xlabel('Distance Along Pipe (ft)');
% title('Pressure Required for Growth Without Buckling');
```

Published with MATLAB® R2022b

Calculate the minimum pressure to retract without buckling

```
close all; clc; clear;
run('data_input.m');
run('growth_pressure.m');
run('growth_without_buckling')

%Constrained retraction
P1r = zeros(1,1600)+(2.*(f_yield + tip_mount_friction))./A; %Pressure required
 to invert without buckling

%Unconstrained retraction
ch = 0; %Counter for unconstrained region
P2r = zeros(1,30); %Allocate storage
for hu = 0:0.1:3 %Loop through heights
    l = hu.*0.3048; %Body length [m]
    ch = ch + 1; %Update counter
    alpha = atan(0.5*D/(l+hv_m)); %Find angle of tail
    p_test = linspace(0,300000,100000); %Setup test pressures and forces
    p_force = p_test.*A;
    r = D./2; %Body radius
    body_w = hu.*w_per_l; %Body mass [kg]
    T_t = (0.5.*p_force +f_yield+tip_mount_friction)./cos(alpha);
    %Moment balance equations:
    LHS = p_test*A*r;
    RHS = tip_weight.*(D.*0.5) + body_w.*(D.*0.5) + ...
        T_t.*(l*sin(alpha)+D*0.5*cos(alpha));
    F_axial = T_t*cos(alpha)+tip_weight+body_w; %Axial Force [N]
    CF = p_force; %Crushing force is equal to pressure force [N]

    %Find Values of pressure that don't cause crushing or axial buckling
    P2r(ch) = min(p_test(CF>=F_axial & LHS>=RHS));
    if isempty(P2r(ch))
        P2r(ch) = 0;
    end
end

%Combine results
Pr = [P1r P2r];
Pr_psi = Pr./6894.76;
SDr = linspace(Lt,L,length(Pr));

% %Plots
% %Figure 5: vertical retraction
% figure;
% plot(SDr,Pr_psi,'LineWidth',lw);
% ylabel('Retraction Pressure (psi)');
% xlabel('Distance Along Pipe (ft)');
% title('Required Retraction Pressure');
% set(gca,"FontSize",20)
```

Calculate the torque and speed required from the motor

```
close all; clc; clear;
run('data_input.m');
run('growth_pressure.m');
run('growth_without_buckling');
run('retraction_without_buckling');

%Estimate diameter of fabric spool
length = linspace(0,(L.*0.3048),length(growth_min_T)); %Length of spool [m]
pf = 2.906; %Packing factor

string_thickness = 4.064e-5; %Thickness of the pull string [m]
r_shaft = 0.004; %Minimum radius of the shaft [m]
d_shaft = 2.*r_shaft;
r_in = sqrt( ((2).*string_thickness.*length(end))./(pi) + (r_shaft.^2) );
%Shaft radius [m]

spool_length = 0.3048; %Length of spool [m]
r_out = sqrt( ((D.*length.*pf.*thickness)./...
    (spool_length)) + (r_in.^2) );
spool_diameter = 2.*r_out; %Diameter of spool [m]

%Estimate motor requirements
tau = flip(growth_min_T).*r_out; %Torque [Nm]
omega = (2.*v)./r_out; %Speed [rad/s]
speed = omega.*9.549297; %Speed [RPM]
power = tau.*omega; %Power [W]

%Estimate safety factor for shaft w/r to yield
%Von mises stress [Pa]
yield_strength = 689; %Yield strength of steel [MPa]
beam_length = 0.6096; %Length of the beam [m]
%Obtained from McMaster
sigma = (4.*growth_min_T.*beam_length)./(pi.*(d_shaft.^3))...
    + sqrt( ((16.*tau)./(pi.*(d_shaft.^3))).^2 +...
    ((4.*growth_min_T.*beam_length)./(pi.*(d_shaft.^3))).^2) );
sigma_max = max(sigma)./(10.^6); %Maximum Von mises stress [MPa]
N_shaft = yield_strength./sigma_max; %Safety factor

% %Figure 7: Motor torque, speed, and power requirements
% figure;
% plot(length,tau,'LineWidth',lw);
% hold on;
% plot(length,speed,'LineWidth',lw);
% hold on;
% plot(length,power,'LineWidth',lw);
% hold on;
% xlabel('Length of Spooled Material (m)');
% ylabel('Torque [Nm], Speed [rpm], Power [W]');
```

11 Appendix E - SOP

Safe Operating Procedure: Vine Robot Inflation

Author:	Rajveer Oberoi, William Heap, Steven Man, Steven Nguyen
Department:	Mechanical Engineering
Building/Room:	Engr 2 Hawkes Lab
Date Approved:	Click or tap to enter a date.

Approved by:	Signature:

1. Description

This SOP describes a test to characterize the growth of a large diameter vine robot that originates from a base station. The base station is comprised of various electronic and mechanical components: motors, pneumatic values, fans, shafts, bearings, and vine robot material. The base station is pressurized and the robot grows through eversion. Multiple subsystems including pneumatics, electronics, and mechanical assemblies work in conjunction for the growth of the robot.

2. Hazards Overview

Example I:

- *Choke Hazard*
  - *While unlikely, the lengthy syl-nylon can pose a choking / suffocation hazard.*
  - *Exercise care, and always keep airways unobstructed*

Example II:

- *Shock*
  - *The base station consists of high voltage electronics.*
  - *Ensure that all loose wires are properly secured, and don't access the electronics box when power supply is plugged in.*
  - *The high voltage electronics box should remain closed when plugged in. If wiring needs to be modified ENSURE that the box isn't plugged into power.*

Example III:

- *Fingers can get caught in rotating shaft*
  - *Keep hands away from the shaft when in operation.*

Example IV:

- *Potentially High Motor Speeds*
  - *Powerful motors can cause components to break away and cause bodily harm. Maintain distance from the base station during use, and wear safety goggles.*

3. Required Personal Protective Equipment (PPE)

Safety Goggles

Closed Toed Shoes

Pants

4. Waste Disposal

Vine Robot Inflation does not produce waste in most cases. In the rare case of component failure, dispose of broken component in nearest trash / recycle bin.

5. Accident and Spill Procedure

- *Minor cuts can be addressed using the Band-Aid station located above the sink.*
- *Seek medical help in the event of significant cuts/injury: Call 911. Notify lab manager.*

The lab manager must be notified in the event of any significant injury. A significant injury is any injury that cannot be addressed by the contents of the room's Band-Aid station.

The lab manager must be notified in the event of a large spill, i.e., greater than 5 gallons, or a spill of any hazardous waste.

6. Equipment

- *Base Station Assembly*

Approver's initials:

_____

- *Vine Robot Fabric*
- *Fan Subassembly*
- *Electronics Box + Power Supply*

7. Approvals Required

Permission of the capstone advisor is required only before the initial run of the procedure.

8. Procedure

1. Setup/Start/Pre-run
    a. Spool Syl-Nylon vine robot body onto the large spool of the motor spool ASM.
    b. Simultaneously clamp both the syl-nylon robot body and the base station bag in between the 2 acrylic plates of the intake ASM
    c. Now, clamp the base station between the two acrylic plates of the backplate ASM: be sure to orient the bag such that the holes align with the
    d. Plug in the 4 cables originating from the Fan Mechanism into the back plate ASM.
    e. Obtain 2 pipe connectors, and fasten them such that they connect the base station to the fan mechanism.
    f. Take 4 U-Channels and attach them to the sides of the base station, be sure to sandwich the bag in between the baseplate and the U-Channels. Engage the clamps.
    g. Ensure there are no loose cables originating from the electronics box, close the cover, and plug it into a wall outlet. Do not open the box while it is connected to power.
2. Process/Run
    a. Utilize the Wi-Fi based user interface to control motor and fan output. Motor 1 corresponds to the fabric spool, and Motor 2 to the ethernet.
    b. Configure settings to rotate the motor 1 on 40% power and motor 2 at 10%.
    c. Use the fan PWM toggle to control airflow into the base station.
    d. Lastly adjust the servo toggle to 70 (Growth Configuration)
    e. Be sure to slowly adjust motor settings as this can be quite jumpy. Play around with UI to ensure that ethernet, vine body, and fan flow are all in sync.
3. Post-Run/Shut-down/Clean-up
    a. Re-Spool Dispensed Syl - Nylon
    b. Unplug and decouple fan mech and electronics asm from the base station
    c. Disengage the U-Channel clamps.

Approver's initials:

_____

References

[1] "Vevor sewer camera system, 200ft." [Online]. Available: https://www.vevor.com/pipe-inspection-camera-c_11031/200ft-pipe-inspection-camera-hd-1200-tvl-drain-sewer-camera-9-lcd-monitor-p_010343652390

[2] "Gpk-32 tracked inspection robot." [Online]. Available: https://www.superdroidrobots.com/store/industries/pest-control/product=2729

[3] "Opticam sewer camera." [Online]. Available: https://usaborescopes.com/products/applications/pipe-inspections/opticam-modular-sewer-inspection-camera/

[4] "Elios 2 price." [Online]. Available: https://www.flyability.com/elios-2-price#:~:text

[5] P. A. der Maur, B. Djambazi, Y. Haberthür, P. Hörmann, A. Kübler, M. Lustenberger, S. Sigrist, O. Vigen, J. Förster, F. Achermann, E. Hampp, R. K. Katzschmann, and R. Siegwart, "Roboa: Construction and evaluation of a steerable vine robot for search and rescue applications," in *2021 IEEE 4th International Conference on Soft Robotics (RoboSoft)*, 2021, pp. 15–20.

[6] M. M. Coad, L. H. Blumenschein, S. Cutler, J. A. R. Zepeda, N. D. Naclerio, H. El-Hussieny, U. Mehmood, J.-H. Ryu, E. W. Hawkes, and A. M. Okamura, "Vine robots," *IEEE Robotics Automation Magazine*, vol. 27, no. 3, pp. 120–132, 2020.

[7] J. Luong, P. Glick, A. Ong, M. S. deVries, S. Sandin, E. W. Hawkes, and M. T. Tolley, "Eversion and retraction of a soft robot towards the exploration of coral reefs," in *2019 2nd IEEE International Conference on Soft Robotics (RoboSoft)*, 2019, pp. 801–807.

[8] E. W. Hawkes, L. H. Blumenschein, J. D. Greer, and A. M. Okamura, "A soft robot that navigates its environment through growth," *Science Robotics*, vol. 2, no. 8, 2017. [Online]. Available: https://www.science.org/doi/abs/10.1126/scirobotics.aan3028

[9] D. A. Haggerty, N. D. Naclerio, and E. W. Hawkes, "Characterizing environmental interactions for soft growing robots," in *2019 IEEE/RSJ International Conference on Intelligent Robots and Systems (IROS)*, 2019, pp. 3335–3342.

[10] W. E. Heap, N. D. Naclerio, M. M. Coad, S.-G. Jeong, and E. W. Hawkes, "Soft retraction device and internal camera mount for everting vine robots," in *2021 IEEE/RSJ International Conference on Intelligent Robots and Systems (IROS)*, 2021, pp. 4982–4988.

[11] M. M. Coad, L. H. Blumenschein, S. Cutler, J. A. R. Zepeda, N. D. Naclerio, H. El-Hussieny, U. Mehmood, J.-H. Ryu, E. W. Hawkes, and A. M. Okamura, "Vine robots," *IEEE Robotics & Automation Magazine*, vol. 27, no. 3, pp. 120–132, 2020.

[12] M. Coad, R. Thomasson, L. Blumenschein, N. Usevitch, E. Hawkes, and A. Okamura, "Retraction of soft growing robots without buckling," 10 2019.

[13] L. H. Blumenschein, A. M. Okamura, and E. W. Hawkes, "Modeling of bioinspired apical extension in a soft robot," in *Living Machines*, 2017.

[14] W. Fichter, U. S. N. Aeronautics, S. Administration, and L. R. Center, *A Theory for Inflated Thin-wall Cylindrical Beams*, ser. A Theory for Inflated Thin-wall Cylindrical Beams. National Aeronautics and Space Administration, 1966, no. v. 3466. [Online]. Available: https://books.google.com/books?id=qav9mWWlb-AC